Identification of dominant DEM parameters for multi-component segregation during heap formation, hopper discharge and chute flow

Hadi, Ahmed; Shi, Hao; Pang, Yusong; Schott, Dingena

DOI
10.1016/j.powtec.2024.119985

Publication date
2024

Document Version
Final published version

Published in
Powder Technology

Citation (APA)
Hadi, A., Shi, H., Pang, Y., & Schott, D. (2024). Identification of dominant DEM parameters for multi-component segregation during heap formation, hopper discharge and chute flow. *Powder Technology*, *444*, Article 119985. https://doi.org/10.1016/j.powtec.2024.119985

Powder Technology 444 (2024) 119985

Contents lists available at ScienceDirect

Powder Technology

journal homepage: www.journals.elsevier.com/powder-technology

Identification of dominant DEM parameters for multi-component segregation during heap formation, hopper discharge and chute flow

Ahmed Hadi *, Hao Shi, Yusong Pang, Dingena Schott

Department of Maritime and Transport Technology, Faculty of Mechanical Engineering, Delft University of Technology, 2628CD Delft, the Netherlands

HIGHLIGHTS

- Sensitivity analysis on 15 DEM interaction parameters to identify dominant ones for segregation.
- Segregation after hopper discharge is mainly influenced by particle-geometry interactions.
- Segregation within the heap is affected by particle-particle interactions as well.
- The dominant DEM parameters are strongly dependent on initial mixture configuration.
- Downstream segregation is highly dependent on upstream segregation dynamics.

GRAPHICAL ABSTRACT

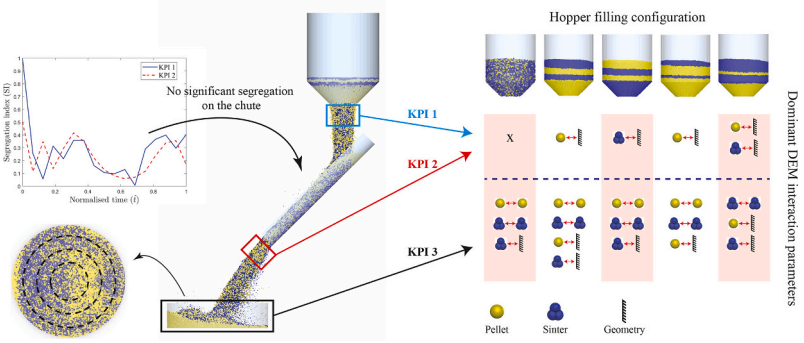

ARTICLE INFO

Keywords:
Granular materials
Segregation
Discrete element method
Sensitivity analysis
Definitive screening design
Pellets and sinter

ABSTRACT

Segregation of granular materials is a critical phenomenon in various industries, such as food processing, pharmaceuticals, and mining. The Discrete Element Method (DEM) is an effective tool for gaining insight into granular segregation by providing particle-level information and the freedom to model mixtures that are often difficult or impossible to achieve through experiments. To ensure realistic material behaviour and correct representation of segregation, it is essential to calibrate the model parameters systematically. However, in the context of multi-component segregation, it is extremely challenging and computationally expensive to consider all parameters in the calibration procedure since interaction parameters between components must also be considered. This work aims to identify the dominant DEM parameters for modelling multi-component segregation during hopper discharge, chute flow and heap formation in a mixture of pellet and sinter. Utilising a representative example of a multi-component mixture with different sizes, densities and shapes used in blast furnaces, the investigation is done for various initial configurations as well as various mass ratios of the mixture. Our findings revealed that, while only particle-geometry interaction parameters dominate the segregation after the hopper and chute flow, particle-particle parameters are also significant for segregation in the heap. We also demonstrated that the downstream segregation is significantly influenced by the segregation upstream. Moreover, we found that the effect of pellet-sinter interactions is negligible. This research provides insights into the dominant DEM parameters, facilitating more efficient and robust calibration of multi-component models in future research endeavours.

* Corresponding author.
E-mail address: a.h.hadi-1@tudelft.nl (A. Hadi).

https://doi.org/10.1016/j.powtec.2024.119985
Received 29 February 2024; Received in revised form 27 April 2024; Accepted 6 June 2024
Available online 8 June 2024

1. Introduction

Granular materials are widely found on Earth and are the second-most handled substances in the industry [1]. Considering the market-driven demand to enhance production, reduce expenses, and develop sustainable products and systems, improving the understanding of the complicated behaviour of granular materials is of great importance [2]. One such behaviour is granular segregation or de-mixing, in which moving particles with similar characteristics (e.g., size or density) gather in specific areas of the mixture. Segregation is mostly considered an undesirable occurrence that negatively impacts the homogeneity of the granular mixtures and, consequently, should be minimised [3].

There are two main types of segregation: size segregation and component segregation [4]. While previous studies have focussed on size segregation in single-component systems [5–16], real-world mixtures are often multi-component, consisting of two or more materials, each with its size distribution, particle density and shape(s) [4], and a few works attempted to model multi-component segregation [17–20]. For example, in the context of a blast furnace, ferrous burden, which is mainly a mixture of iron ore pellets and sinter, is loaded into the blast furnace. The component segregation in the furnace throat can reduce the permeability of the burden, leading to inefficient use of reductant gas and causing economic and environmental consequences [10,14]. Therefore, understanding the segregation behaviour of multi-component granular mixtures is essential towards efficient and sustainable processes.

Segregation has been experimentally investigated since the early '70s [21–24]. The primary objective was to unravel the mechanisms behind the separation of components within mixtures during various types of agitation [21], subsequently developing mathematical models to capture these phenomena. A common approach is to study the effect of individual material properties by isolating other properties, e.g., considering material mixtures differing only in size [24] or density [22], and eventually, the combined impact of both size and density [23]. Such a methodical approach enabled researchers to incorporate the influence of each material property within mathematical models. However, experimental approaches come with several limitations [4]. Firstly, acquiring data on the composition of a granular mixture is impeded by several challenges. These include sampling difficulties, the complications involved in separating components of similar size within the multi-component mixture, and the opaqueness of the particles making the inner structure of the granular system not observable [25]. Secondly, it is nearly impossible to obtain particle-scale information such as contact

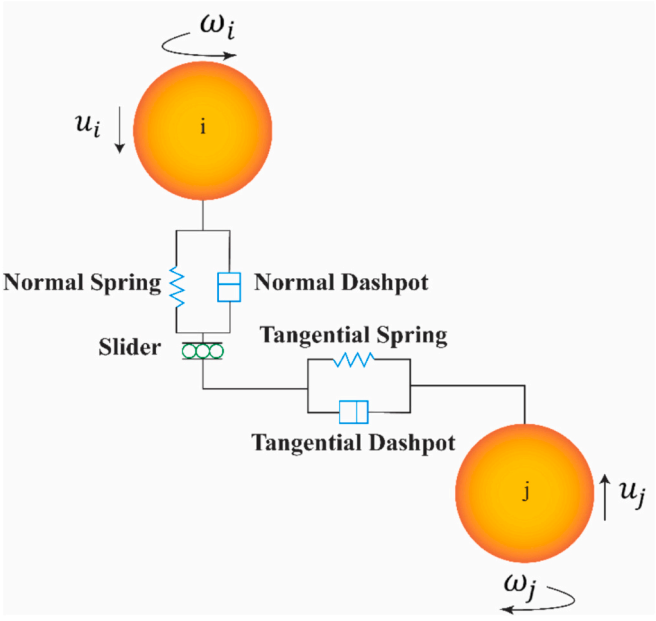

Fig. 1. A schematic definition of interaction forces between two particles in DEM.

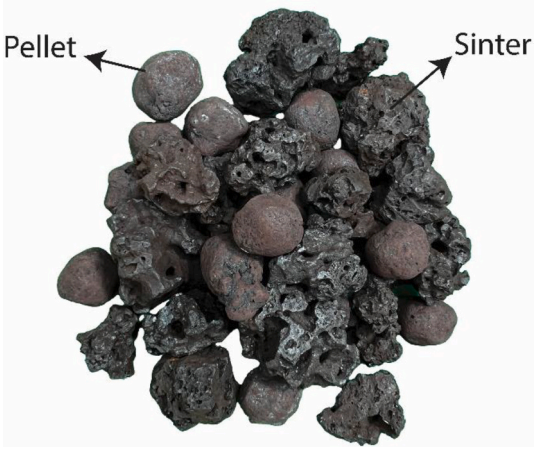

Fig. 2. A mixture of pellets and sinter.

Table 1
Intrinsic material properties used in DEM simulations.

DEM Parameter	Pellet	Sinter	Geometry
Shear modulus (G)	1e+8 Pa [37]	1e+8 Pa [37]	2e+11 Pa [41]
Poisson's ratio (υ)	0.25 [37]	0.25 [37]	0.3 [41]
Solid density (ρ_s)	1951 (kg/m^3)	1731 (kg/m^3)	7800 (kg/m^3) [41]

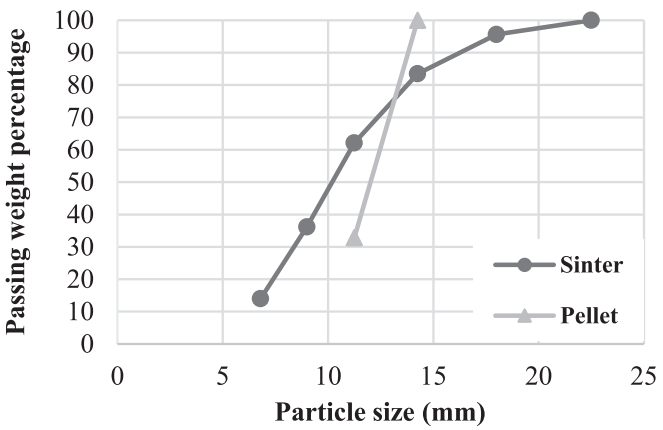

Fig. 3. Particle size distribution (PSD) for pellets and sinter [40].

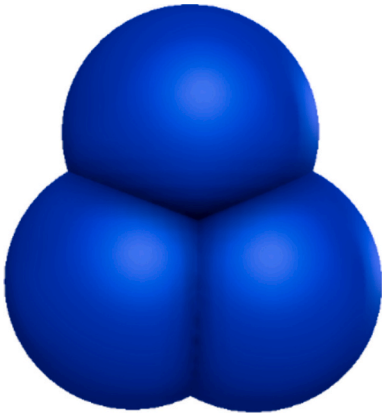

Fig. 4. The clumped spheres model used to simulate sinter particles.

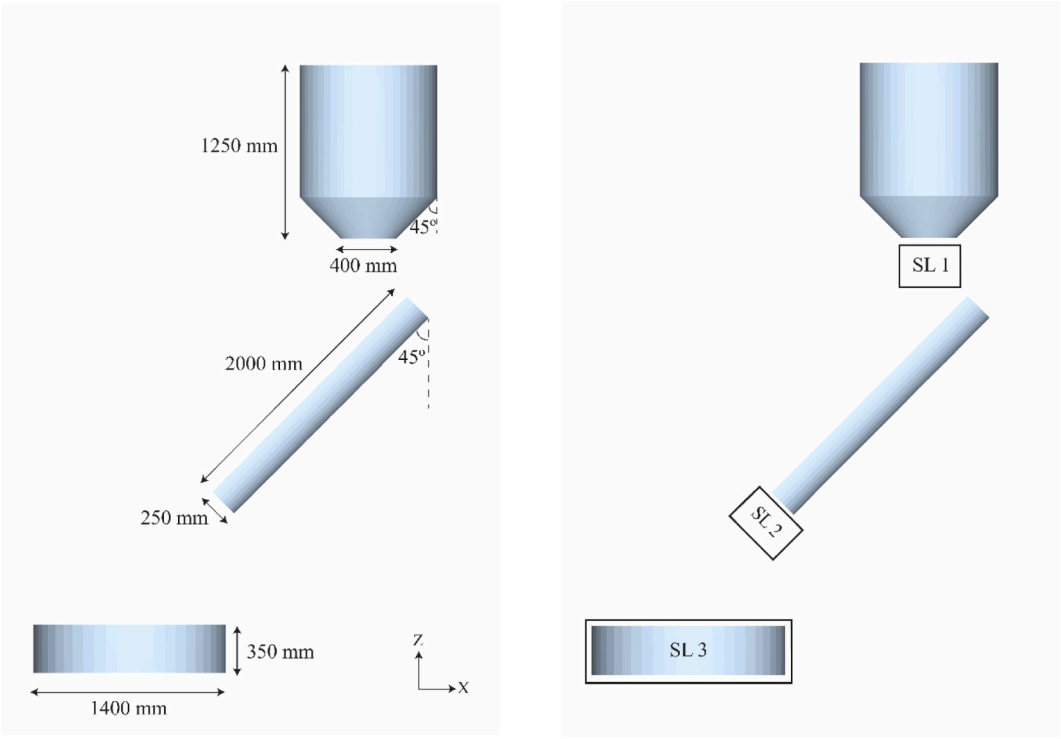

Fig. 5. a) The geometries used in the simulations and their dimensions, and b) cylindrical sampling locations (SLs) used to quantify segregation.

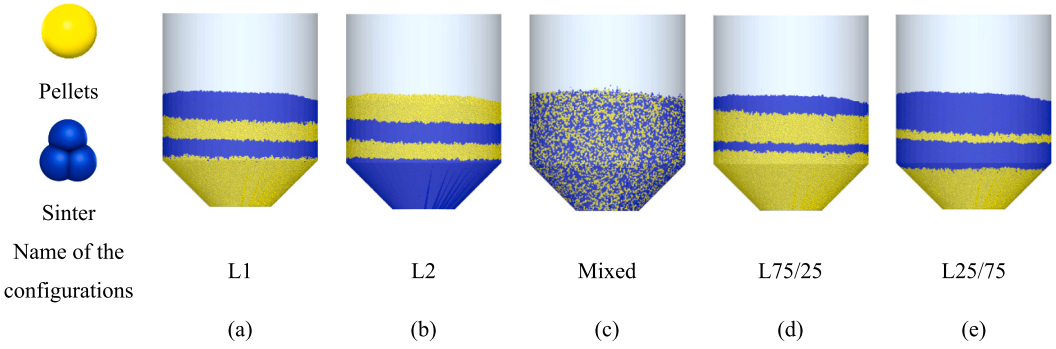

Fig. 6. Various hopper filling configurations used in the simulations (yellow and blue particles represent pellets and sinter, respectively). (For interpretation of the reference colour in this figure legend, the reader is referred to the web version of this article.)

force chains to elucidate macro-scale bulk behaviour. Lastly, conducting comprehensive experimental studies to investigate various factors using tons of materials is costly and time-consuming.

With the development of computational power in the last decades, the Discrete Element Method (DEM), first introduced by Cundall and Strack [26], has become a widely used approach to simulate granular materials. DEM involves iteration over several time steps, within each, Newton's second law of motion is used to update particle trajectories, while contact models are used to compute forces due to interparticle and particle-geometry interactions. DEM offers significant advantages over experiments for investigating the segregation, as it not only allows the modelling of mixtures of particles with any combination of size, density and shape but also provides detailed particle-level information that is hardly acquirable in experiments.

Although DEM is extensively used, there are still various challenges to be solved, mainly related to computational efficiency (i.e. feasibility) and model accuracy (i.e. reliability) [27]. Achieving a balance between computational efficiency and model accuracy requires making trade-offs between conflicting interests i.e. feasibility and reliability. Several solutions such as reducing particle stiffness [28] and employing upscaled particles [29,30] have been proposed to enhance the computational efficiency of DEM. However, the reliability of the developed model heavily depends on the proper determination (calibration) of the input parameters of the modified particles. This process can be time-consuming, particularly in complex multi-component mixtures with a high number of parameters. To tackle this issue, the calibration can be focused on only the "significant" parameters. Several previous researchers have attempted to identify the most significant parameters for segregation [10,31–33]. However, these studies have several shortcomings. Firstly, they primarily investigated size segregation and the dominating parameters for component segregation are missing. Secondly, none of these studies has included all DEM interaction parameters, i.e., both particle-particle and particle-geometry interactions, thus the true/relative significance of these parameters remains unknown.

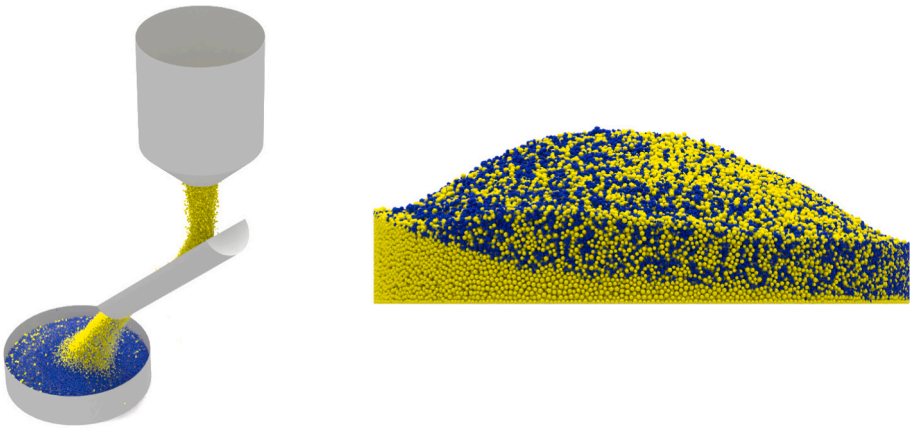

(a) (b)

Fig. 7. a) Materials flowing from the hopper to the receiving bin through the chute, b) an example of the heap formed in the receiving bin.

Table 2
Investigated DEM parameters using the definitive screening design with their low, middle and high values. (μ_s = coefficient of sliding friction, μ_r = coefficient of rolling friction, C_r = coefficient of restitution. The underlined values for pellet-pellet and sinter-sinter parameters used for pellet-sinter interactions.)

Factor		Low level (−1)	Middle level (0)	High level (+1)
Pellet-pellet	$\mu_{s,pp}$	0.21 [7]	0.455	0.7 [51]
	$\mu_{r,pp}$	0.05 [52]	0.145	0.24 [41]
	$C_{r,pp}$	0.3 [53]	0.5	0.7 [10]
Sinter-sinter	$\mu_{s,ss}$	0.43 [54]	0.595	0.76 [41]
	$\mu_{r,ss}$	0.08 [37]	0.23	0.38 [41]
	$C_{r,ss}$	0.01 [55]	0.18	0.35 [41]
Pellet-sinter	$\mu_{s,ps}$	0.21	0.485	0.76
	$\mu_{r,ps}$	0.05	0.215	0.38
	$C_{r,ps}$	0.01	0.355	0.7
Pellet-geometry	$\mu_{s,pg}$	0.31 [53]	0.405	0.5 [56]
	$\mu_{r,pg}$	0.05 [53]	0.2	0.35 [51]
	$C_{r,pg}$	0.2 [10]	0.41	0.62 [41]
Sinter-geometry	$\mu_{s,sg}$	0.38 [36]	0.64	0.9 [12]
	$\mu_{r,sg}$	0.08 [37]	0.14	0.2 [36]
	$C_{r,sg}$	0.05 [12]	0.275	0.5 [55]

Thirdly, segregation is only studied in a single geometry while its behaviour can vary during different stages/geometries in a full process. Lastly, conflicting findings regarding the significance of certain DEM parameters have been reported in some cases [10,31]. To address these gaps, in this study, we aim to perform a comprehensive sensitivity analysis to gain deeper insights into the significant DEM parameters for multi-component segregation in various geometries, including hopper discharge, chute flow and heap formation, which represent the typical burden charging process in the blast furnace. We show this for a mixture of iron ore pellets and sinter which are charged into the blast furnace as ferrous burden with a focus on interaction parameters such as sliding and rolling friction. We also conducted a sensitivity study for various initial configurations of pellets and sinter to identify the dominant parameters for different hopper filling configurations. Additionally, we extended our study to investigate the effect of several factors, i.e. the shape of sinter particles and the mass ratio of pellets to sinter, on the segregation that occurs at different locations, i.e. after the hopper, after the chute and in the heap.

This paper is structured as follows. In Section 2, we provide an in-depth explanation of the method employed, i.e. the Discrete Element Method (DEM), detailing the simulated materials and their fixed DEM parameters as well as the setups used for investigating segregation. Section 3 explains the design of experiments (DoE) employed in this study. We discuss the varied DEM parameters in the DoE aimed at identifying the dominant ones, along with the key performance indicators (KPIs) quantified and employed as responses in the DoE. In Section 4, we present our findings regarding the dominant DEM parameters for segregation as well as the effect of certain factors (i.e., the shape of sinter particles and the mass ratio of pellets to sinter) on segregation occurring at different locations. Finally, in Section 5 we conclude with our main findings and further work.

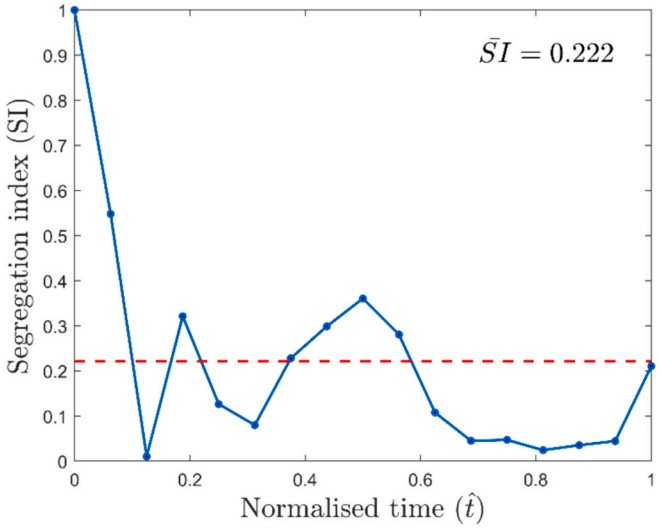

Fig. 8. An example of the segregation index as a function of the normalised time (Run 36 with L1 initial configuration). The red dashed line indicates "SI bar ". (For interpretation of the references to colour in this figure legend, the reader is referred to the web version of this article.)

2. Materials and methods

2.1. Discrete element method

Our DEM model employs the Hertz-Mindlin (no-slip) [34] contact model with an elastic-plastic spring-dashpot rolling friction model (type C according to Ai et al. [35]) that has been successfully applied in previous studies modelling iron ore pellets and sinter [36,37]. Fig. 1 provides a schematic representation of the interaction forces between two particles in DEM. For detailed equations and further information on the contact model, readers are referred to the relevant literature

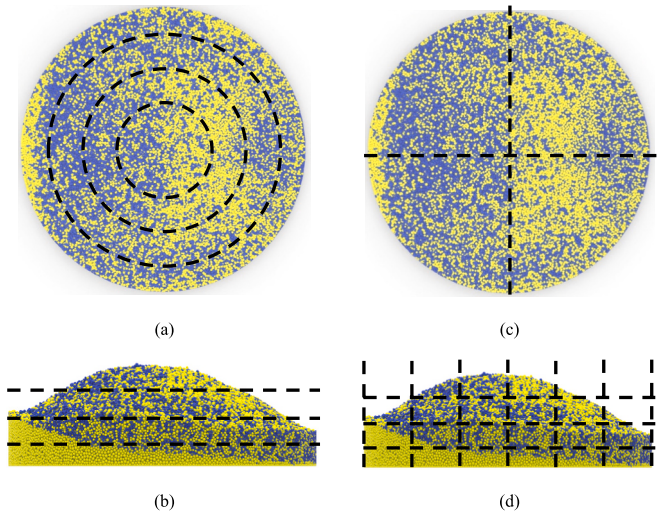

Fig. 9. Different grid systems to measure the segregation within the heap, a) radial, b) vertical, c) circumferential and d) cubic.

Table 3
p-values for the effect of DEM interaction parameters on KPI 1 for various hopper filling configurations, with the effect of each significant parameter on KPI 1 in parentheses (e.g., "(+)" denotes that with an increase in the parameter value, KPI 1 increases.). "x" means insignificant effect.

Factor		Mixed	L1	L2	L75/25	L25/75
Pellet-pellet (P-P)	$\mu_{s,pp}$	x	x	x	x	x
	$\mu_{r,pp}$	x	x	x	x	x
	$C_{r,pp}$	x	x	x	x	x
Sinter-sinter (S-S)	$\mu_{s,ss}$	x	x	x	x	x
	$\mu_{r,ss}$	x	x	< 0.0001 (+)	x	x
	$C_{r,ss}$	x	x	x	x	x
Pellet-sinter (P-S)	$\mu_{s,ps}$	x	x	x	x	x
	$\mu_{r,ps}$	x	x	x	x	x
	$C_{r,ps}$	x	x	x	x	x
Pellet-geometry (P-G)	$\mu_{s,pg}$	x	< 0.0001 (+)	x	< 0.0001 (+)	0.0003 (−)
	$\mu_{r,pg}$	x	< 0.0001 (+)	x	< 0.0001 (+)	< 0.0001 (−)
	$C_{r,pg}$	x	x	x	x	x
Sinter-geometry (S-G)	$\mu_{s,sg}$	x	x	< 0.0001 (+)	x	0.005 (−)
	$\mu_{r,sg}$	x	x	x	x	x
	$C_{r,sg}$	x	x	x	x	x

[34–36,38]. We used the commercial software EDEM version 2022.3 to develop the DEM model and we conducted all simulations on the DelftBlue high-performance cluster [39].

2.2. Simulation configuration

2.2.1. Materials and fixed DEM parameters

We simulate the mixture of iron ore pellets and sinter (cf. Fig. 2), which is a good example of a real-world multi-component mixture charged into the blast furnace. For modelling pellets and sinter in DEM, we used fixed parameter values for intrinsic material properties (Table 1) as well as for morphological parameters, including particle shape and particle size distribution. Particle densities for pellets and sinter were calibrated against their bulk densities in our previous work [40]. Moreover, we measured particle size distribution using sieves in the same work, as illustrated in Fig. 3.

For particle shape, spheres are well-suited for pellets since they are nearly spherical. However, sinter particles are highly irregular in shape

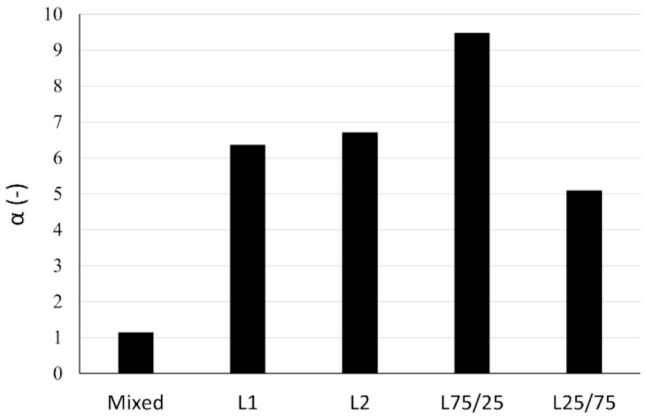

Fig. 10. The value of α (cf. Eq. (5)) for the initial configurations presented in Fig. 6.

(cf. Fig. 2), requiring a non-spherical representation for segregation modelling [13]. Here, we adopt a clumped sphere approach to represent the irregular shape of sinter particles. As increasing the number of spheres in the clumped sphere significantly increases the computational time, a three-sphere clumped particle is chosen as shown in Fig. 4, which has yielded good results in previous sinter studies [12,37]. A detailed overview of all DEM input parameters can be found in Table A1 in Appendix A.

2.2.2. System and geometry

A set of geometries is employed, which consists of a hopper, a chute and a receiving bin to investigate and quantify the segregation at various stages (i.e., after hopper discharge, after chute flow and during heap formation) within a single system. Fig. 5a schematically illustrates the geometries and their dimensions. Additionally, we created three cylindrical sampling locations (SLs) right after the hopper and chute as well as around the heap to measure segregation, as shown in Fig. 5b.

The initial mixture of pellets and sinter is generated within the hopper with an equal mass ratio of 50%–50%. To examine the effect of different initial configurations of pellets and sinter, we used various initialisations within the hopper, as shown in Fig. 6a-c. Notably, the difference between L1 (cf. Fig. 6a) and L2 (cf. Fig. 6b) lies in the order of pellets and sinter layers. Moreover, to study the impact of the mass ratio, we defined two additional cases with the pellets-to-sinter mass ratios of 75%–25% and 25%–75%, as illustrated in Fig. 6d and Fig. 6e, respectively.

Following generating the mixture within the hopper, we opened the hopper outlet, allowing the materials to discharge under the influence of gravity, as shown in Fig. 7a. It is important to note that we designed the hopper's geometry in a way to ensure a consistent core flow under all circumstances to have a mixed flow. Subsequently, these materials were charged into the receiving bin via a chute featuring a semi-circular intersection to form a heap. Fig. 7b provides a side view example of the heap formed in the receiving bin.

3. Design of experiment

DoE is employed to efficiently explore the relationship between certain input variables and one or more outputs (or responses). Screening designs, a subset of DoE are helpful in identifying the most significant variables for a given response. Three main types of screening designs are frequently used: fractional factorial [42,43], Plackett-Burman (PB) [44,45] and definitive screening design (DSD) [46–48]. In this study, we choose the definitive screening design as it requires a relatively small number of runs. We used JMP® 17 Pro software (SAS Institute, USA) to design the DSD.

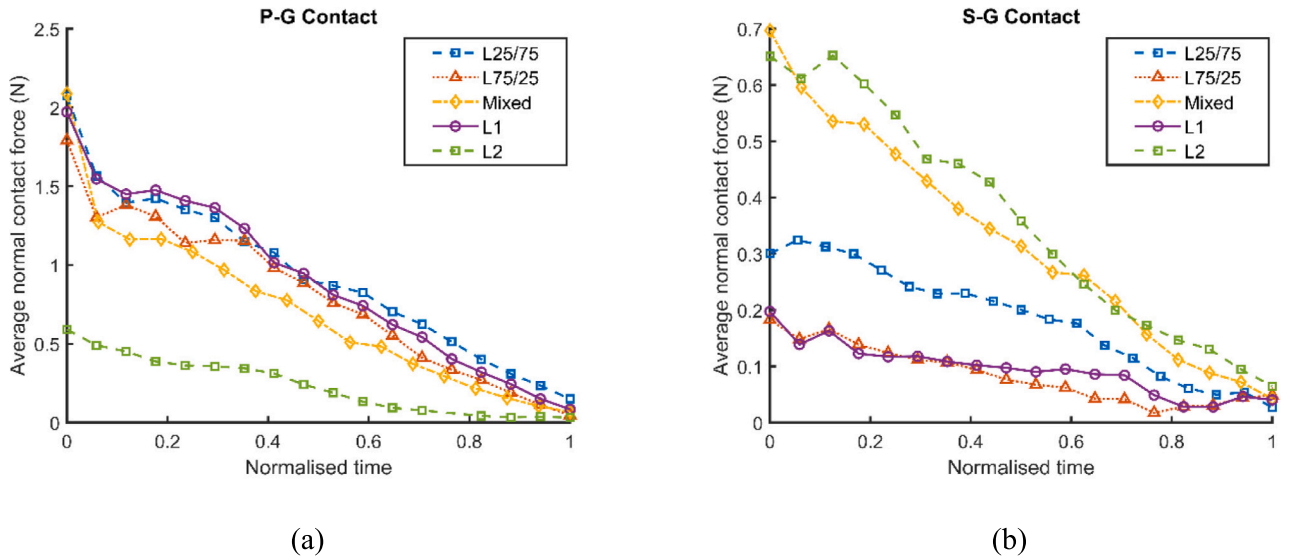

Fig. 11. Average contact force within the hopper for different types of contact in various initial configurations (P-G: pellet-geometry/ S-G: sinter-geometry).

3.1. Definitive screening design

We employed the DSD, a novel three-level design introduced by Jones and Nachtsheim [49]. DSD can detect not only the main effects but also two-factor and quadratic terms. DSD offers an advantage over the PB design in that main effects are not confounded with two-factor interactions, two-factor interactions are not fully confounded with each other, and quadratic effects are not confounded with other two-factor interactions [46]. The number of runs required for k variables is $2k+1$ for even k and $2k+3$ for odd k. Moreover, Jones and Nachtsheim [50] recommended adding four extra runs to enhance the power of the design. Upon conducting the DSD, the p-values of the variables are determined by fitting a model. These p-values reflect the validity of the null hypothesis, which assumes no effect of the variables on the response. In other words, a lower p-value indicates a greater likelihood that the corresponding variable has a significant effect on the response. Therefore, variables with p-values less than a pre-defined threshold can be considered statistically significant.

3.2. Investigated parameters and levels

The parameters investigated in this study include all the interaction parameters for particle-particle and particle-geometry contacts. Table 2 provides a list of these parameters (15 in total) along with their corresponding low and high levels. We select these low and high levels based on a thorough review of the relevant literature, and the middle level (0) is the average between low and high values. In the absence of literature on pellet-sinter interaction, we established the low and high levels for pellet-sinter interactions by using the minimum and maximum values obtained from pellets and sinter interactions, which are underlined in Table 2. In our study, where we investigate 15 parameters, DSD requires 37 runs, as outlined in Table B1. We conducted three repetitions of the simulations to account for the variability arising from the stochastic nature of DEM.

3.3. Quantifying segregation

3.3.1. Segregation after hopper discharge (KPI 1) and chute flow (KPI 2)

The segregation of pellets and sinter after the hopper discharge (KPI 1) and after chute flow (KPI 2) are a function of time. To resemble the stop-start sampling method used by Standish and Kilic [57], we used two cylindrical sampling spaces located right after the hopper (SL1) and chute (SL2) (cf. Fig. 5b). We then proceeded to measure the mass of the pellets (W_p) and sinter (W_s) within the sample space every 0.2 s. We then defined the segregation index (SI) as:

$$SI = \frac{|\chi_p - \chi_0|}{|\chi_{max} - \chi_0|} \tag{1}$$

where $\chi_p = W_p/(W_p + W_s)$ is the instantaneous mass ratio of pellets within the sample, χ_0 is the initial mass ratio of pellets in the hopper and χ_{max} is the maximum mass ratio possible which is always equal to 1. Fig. 8 presents a typical example of SI over time. To minimise the error, we restricted the mass ratio measurements to instances when the total mass within the sampling space exceeded 20% of the full state, i.e. to determine t_{min} and t_{max}. We then normalised the time values using the following equation:

$$\hat{t}_i = \frac{t_i - t_{min}}{t_{max} - t_{min}} \tag{2}$$

where t_i and $\hat{t}_i$ are the instantaneous time and its corresponding normalised time, respectively. Finally, we calculated the mean value of the SIs (i.e. $\overline{SI}$) across the normalised time:

$$\overline{SI} = \frac{\sum_{i=1}^{n} SI_i}{n} \tag{3}$$

where n is the number of data points in Fig. 8, SI_i is the segregation index at ith normalised time (i.e. at $\hat{t}_i = (i-1)*((t_{max} - t_{min})/n)$). We used $\overline{SI}$, which is denoted as the red dashed line in Fig. 8, to quantify KPI 1 and KPI 2.

3.3.2. Segregation in the heap (KPI 3)

Unlike KPI 1 and KPI 2, which involved segregation over a period of time, we measure KPI 3 in a static heap (SL3) at the end of the simulations using the relative standard deviation (RSD). This grid-dependent index is determined by initially defining a grid system to partition the heap into a specified number of bins, denoted as 'm'. Within each bin, the mass ratio of one component such as pellets (C_{p_m}) is measured. Afterwards, the standard deviation (σ) and mean (μ) of C_{p_m}s are computed and finally, RSD is calculated using the following equation:

$$RSD = \frac{\sigma}{\mu} \tag{4}$$

Segregation in the heap can occur in different directions, i.e. radial,

(a)

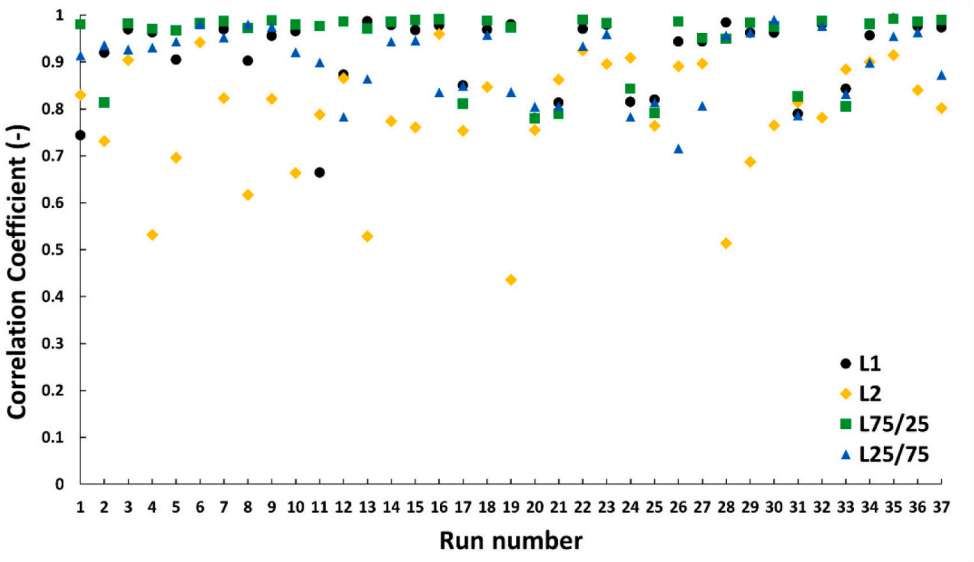

(b)

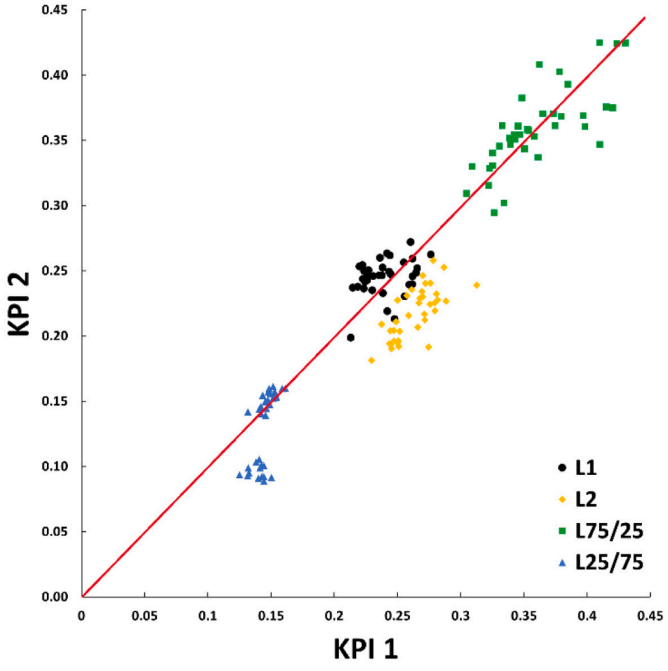

Fig. 12. a) Correlation coefficients between KPI 1 and KPI 2 (i.e. segregation after the hopper and after chute flow, respectively) for all initial configurations across all runs, and b) The relationship between KPI 2 and KPI 1 (red line represents the line of equality). (For interpretation of the references to colour in this figure legend, the reader is referred to the web version of this article.)

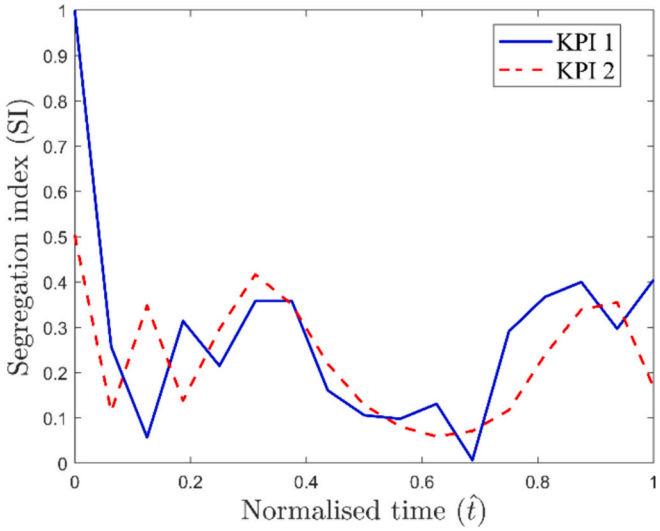

Fig. 13. Comparison of segregation plots of KPI 1 and KPI 2 (i.e. segregation after the hopper and after chute flow, respectively) for the run with the lowest found correlation ~0.40 (Run 19 with L2 hopper filling configuration).

vertical, circumferential as well as throughout the whole volume. Therefore, we assessed KPI 3 by employing four distinct grid systems: radial, vertical, circumferential and cubic grids, as illustrated in Fig. 9a-d, respectively.

4. Results and discussion

We present and discuss the results in two sub-sections. In Section 4.1, we highlight our findings regarding the dominant DEM parameters for each KPI. In Section 4.2, we shift our focus to the effect of several factors, including sinter particle shape, layering mode, and pellets-sinter mass ratio on KPIs. Finally, we present a summary of the findings of this study in Section 4.3.

4.1. Identification of dominant DEM parameters

We followed several steps to identify the dominant parameters for each KPI (refer to Section 3.3). Firstly, we conducted all the necessary simulations with the specified parameters as outlined in Table B1. Secondly, we processed the data and computed the values for each KPI. Thirdly, we utilized the "fit definitive screening" platform in JMP® Pro for performing the Design of Experiments (DoE). In JMP Pro software, we employed the stepwise regression method with a *p*-value threshold of 0.01. Finally, we conducted an analysis of variance (ANOVA) to determine the *p*-values of the significant parameters and considered the variables with p-values lower than 0.01 as statistically significant. The findings for KPI 1 and KPI 2 (i.e., segregation after the hopper and chute in sampling locations shown in Fig. 5b) are presented in Section 4.1.1 and 4.1.2, respectively. Additionally, the results for KPI 3 (i.e., segregation in the heap, illustrated in Fig. 9) are discussed in Section 4.1.3.

4.2. Segregation after hopper discharge (KPI 1)

Table 3 displays the p-values derived from ANOVA analysis of the DSD for KPI 1. Two key observations arise from Table 3. Firstly, there are no significant DEM interaction parameters for the mixed initial configuration. Secondly, for all other initial configurations, pellet-geometry and/or sinter-geometry interaction parameters are dominant.

We elaborate on the first observation as follows. As mentioned in Section 3.2, we conducted 37 simulations (cf. Table B1) with three repetitions to account for the stochastic nature of DEM. The stochastic nature of DEM, due to variations in the generated particles' positions and orientations, could lead to different degrees of mixing within the hopper, significantly influencing the segregation afterwards [31,58]. Therefore, the variation in $\overline{SI}$ across the runs may primarily result from random degrees of mixing within the hopper rather than variations in DEM parameters. To quantitatively assess this, we compared the standard deviation resulting from the three repetitions with the standard deviation of the mean $\overline{SI}$ values for the 37 runs. We carried out this comparison using Eq. (5):

$$\alpha = \frac{\sigma(\mu(\overline{SI}))}{\overline{\sigma_{reps}}} \tag{5}$$

where $\sigma(\mu(\overline{SI}))$ is the standard deviation of the mean $\overline{SI}$ (i.e., mean segregation index calculated using Eq. (3)) across 37 runs, and $\overline{\sigma_{reps}}$ represents the average of standard deviation resulting from the three repetitions for each run. If the value α approaches 1.0, it indicates that alterations in $\overline{SI}$ across the runs primarily stem from the random degree of mixing within the hopper and not from varying the DEM parameters. Fig. 10 illustrates the coefficient α corresponding to various initial configurations for KPI 1. As expected, the value of α for the mixed configuration is close to 1.0 and is significantly lower than the value for other initial configurations. Additionally, the sheer amount of segregation occurring for the mixed configuration is negligible (i.e. $\overline{SI} \leq 0.014$).

The second observation is that, based on the *p*-values, KPI 1 is predominantly influenced by particle-geometry interaction parameters. However, as mentioned earlier, the p-value only addresses the validity of the null hypothesis (i.e., the assumption of no effect of the variables) rather than directly showing the parameters' significance [59]. To validate these findings, we complemented the statistical analysis with physics-based interpretations through a supplementary contact data analysis. This involved extracting the average contact force for each contact type (e.g., the pellet-geometry contact) by dividing the

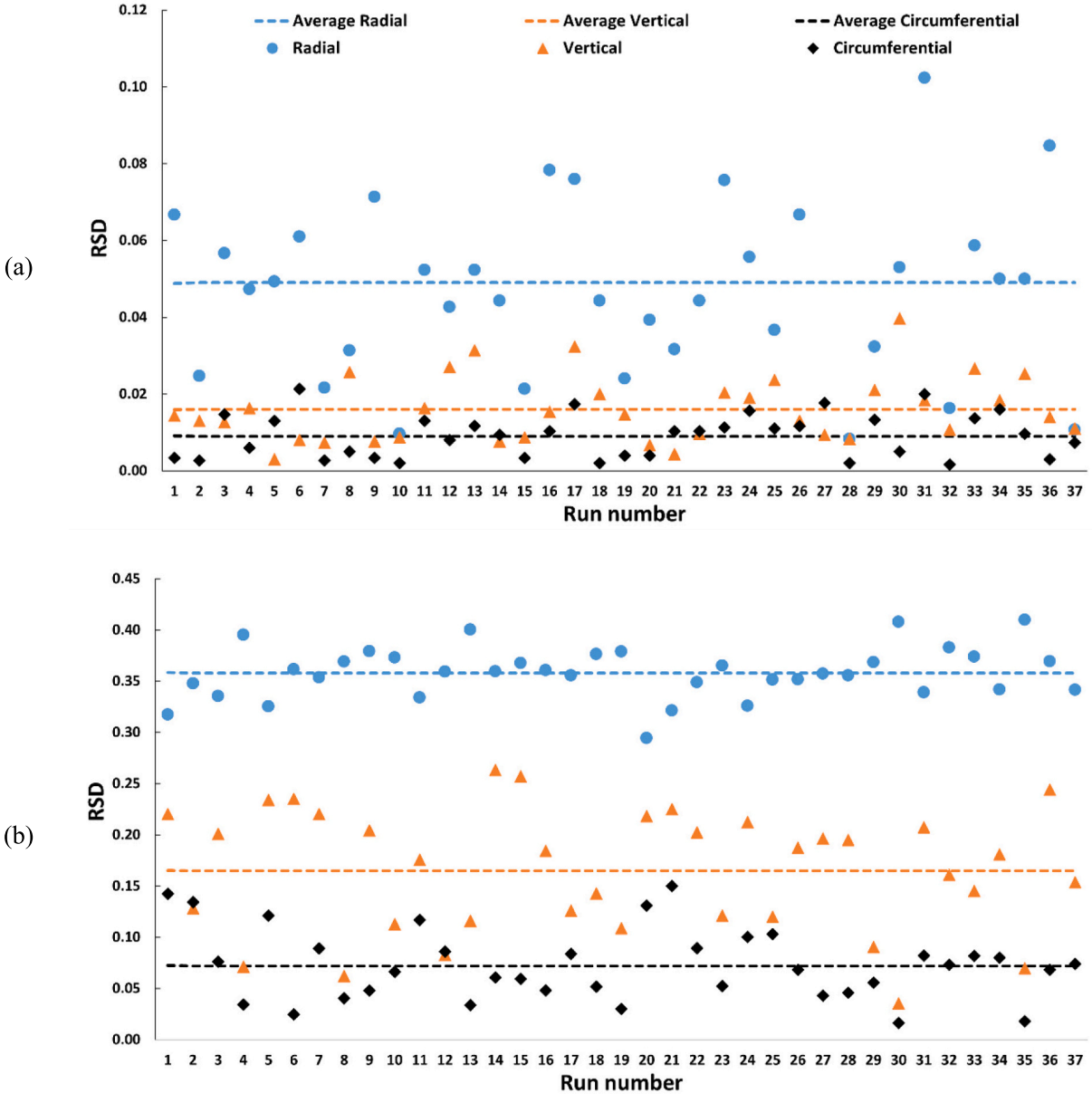

Fig. 14. Comparison of RSDs in the radial, vertical and circumferential directions of the heap across all runs for a) mixed and b) L1 configurations within the hopper (the dashed lines represent the average RSD across the runs).

Table 4
P-values for all DEM parameters for KPI 3 (i.e., radial segregation in the heap) across various initial configurations, with the effect of each significant parameter on KPI 3 in parentheses (e.g., "(+)" denotes that with an increase in the parameter value, KPI 3 increases| "x" means no significant effect).

Factor \ initial configurations		Mixed	L1	L2	L75/25	L25/75
Pellet-pellet (P-P)	$\mu_{s,pp}$	0.0038 (+)	x	x	x	x
	$\mu_{r,pp}$	x	0.0004 (−)	0.009 (+)	0.0012 (−)	x
	$C_{r,pp}$	x	x	x	x	x
Sinter-sinter (S-S)	$\mu_{s,ss}$	< 0.0001 (−)	< 0.0001 (−)	0.0007 (+)	< 0.0001 (−)	< 0.0001 (−)
	$\mu_{r,ss}$	x	x	x	x	x
	$C_{r,ss}$	x	x	x	x	x
Pellet-sinter (P-S)	$\mu_{s,ps}$	x	x	x	x	x
	$\mu_{r,ps}$	x	x	x	x	x
	$C_{r,ps}$	x	x	x	x	x
Pellet-geometry (P-G)	$\mu_{s,pg}$	x	< 0.0001 (−)	x	< 0.0001 (−)	< 0.0001 (−)
	$\mu_{r,pg}$	x	< 0.0001 (−)	x	< 0.0001 (−)	x
	$C_{r,pg}$	x	x	x	x	x
Sinter-geometry (S-G)	$\mu_{s,sg}$	< 0.0001 (+)	< 0.0001 (−)	< 0.0001 (−)	x	< 0.0001 (−)
	$\mu_{r,sg}$	x	x	x	x	x
	$C_{r,sg}$	x	x	x	x	x

aggregate contact force by the total number of contacts of that specific type at each time step within the hopper. We chose average contact force as our metric because the segregation of two components arises from differences in their velocities, which, in turn, result from varying forces acting on them in the DEM simulation. This systematic approach facilitates the identification of the relative contributions of individual contact types to the dynamics of the flow, allowing us to assign significance based on their respective contributions.

Fig. 11 presents the average contact force for two significant contact types based on Table 3, i.e. pellet-geometry and sinter-geometry interactions, across various initial configurations (cf. Fig. 6). We note that using clumped spheres for sinter particles allows for multiple simultaneous contacts with the geometry, leading to lower absolute normalised force values for sinter-geometry compared to pellet-geometry contacts, as reflected in Fig. 11. We also included the mixed configuration for the sake of comparison.

Fig. 11a shows that the average pellet-geometry (P-G) contact force for L2 initial configurations is lower compared to other configurations. This confirms the ANOVA analysis findings in Table 3, highlighting the dominance of pellet-geometry (P-G) interaction parameters across all initial configurations except for L2. This exception can be attributed to the different layering composition of L2, where the bottom layer which has extensive contact with the bottom part of the hopper, primarily consists of sinter particles. Similarly, regarding sinter-geometry interaction, Fig. 11b shows that the average sinter-geometry (S-G) contact force for the configurations L2 is higher than the rest, consistent with the *p*-values in Table 3. However, for L25/75, the average contact force is lower than the mixed configuration, indicating a reduced significance of sinter-geometry interaction parameters. This observation is also reflected in Table 3, where S-G interaction parameters exhibit the highest p-value. Overall, this supporting observation confirms that the results of the ANOVA analysis are also valid from physics-based observations.

By comparing the p-values in Table 3 between various cases, we draw more conclusions regarding the impact of layering mode and mass ratio on the dominant parameters. Regarding the layering mode, we deduce that interaction parameters between the particles at the bottommost layer and the hopper play a key role. In other words, in L2, where the bottom particles consist of only sinter, sinter-geometry interactions dominate, whereas in the L1 case, pellet-geometry interactions are significant. These conclusions are also reflected in Fig. 11a, where the average pellet-geometry contact force in L1 is higher than in L2, while the opposite trend is observed for the sinter-geometry contact force in Fig. 11b.

When comparing the L1, L75/25 and L25/75, we note that the effect of the pellet-sinter mass ratio is twofold. Firstly, it influences the dominant parameters, e.g., by increasing the sinter mass ratio to 0.75 (i.e., L25/75), the sinter-geometry coefficient of static friction becomes significant. This is because in this case, as shown in Fig. 11b, the average sinter-geometry contact force, in L25/75 is significantly higher compared to both L1 and L75/25 configurations. Secondly, while in L25/75, an increase in the pellet-geometry coefficients of rolling and static friction ($\mu_{r,pg}$ and $\mu_{s,pg}$) leads to a reduction in segregation after hopper discharge, this is reversed in all other initial configurations.

4.2.1. Segregation after chute flow (KPI 2)

Before continuing with KPI 2, we first compared the segregation occurrence after the hopper discharge (KPI 1) and following the chute flow (KPI 2) to assess potential significant segregation occurring in between, i.e. on the chute itself. To quantitatively evaluate the similarity between KPI 1 and KPI 2, we calculated the coefficient of correlation (R) of segregation indices (SIs) for each run between KPI 1 and KPI 2 using the following equation:

$$R = \frac{1}{N-1}\sum_{i=1}^{N}\left(\frac{SI_i^1 - \overline{SI^1}}{\sigma_{SI^1}}\right)\left(\frac{SI_i^2 - \overline{SI^2}}{\sigma_{SI^2}}\right) \tag{6}$$

where SI_i^1 and SI_i^2 denote the segregation indices (SIs) at ith normalised time (i.e. at $\widehat{t}_i = (i-1)*((t_{max} - t_{min})/n)$) in the plots of KPI 1 and KPI 2 (cf. Fig. 8), respectively. Fig. 12a presents the correlation coefficients for all initial configurations across all runs. Here, we excluded the mixed initial configurations for the same reasons mentioned in Section 4.1.1. It shows that for most runs, the correlation coefficient is higher than 0.7, indicating a strong correlation between KPI 1 and KPI 2 [60]. To further confirm this strong correlation, we plotted KPI 2 against KPI 1, as shown in Fig. 12b. Notably, most of the runs align closely with the line of equality, indicating a robust linear correlation between KPI 2 and KPI 1.

To examine differences between KPI 1 and KPI 2 for the runs with low correlation coefficients as well as the runs falling below the line of equality in Fig. 12b (e.g. a group of blue triangles), we compare the plots for run 19 with the L2 initial configuration, which has the lowest correlation coefficient (~ 0.4) in Fig. 12a. The segregation plots for KPI 1 and KPI 2 are displayed in Fig. 13. It demonstrates that, despite a low

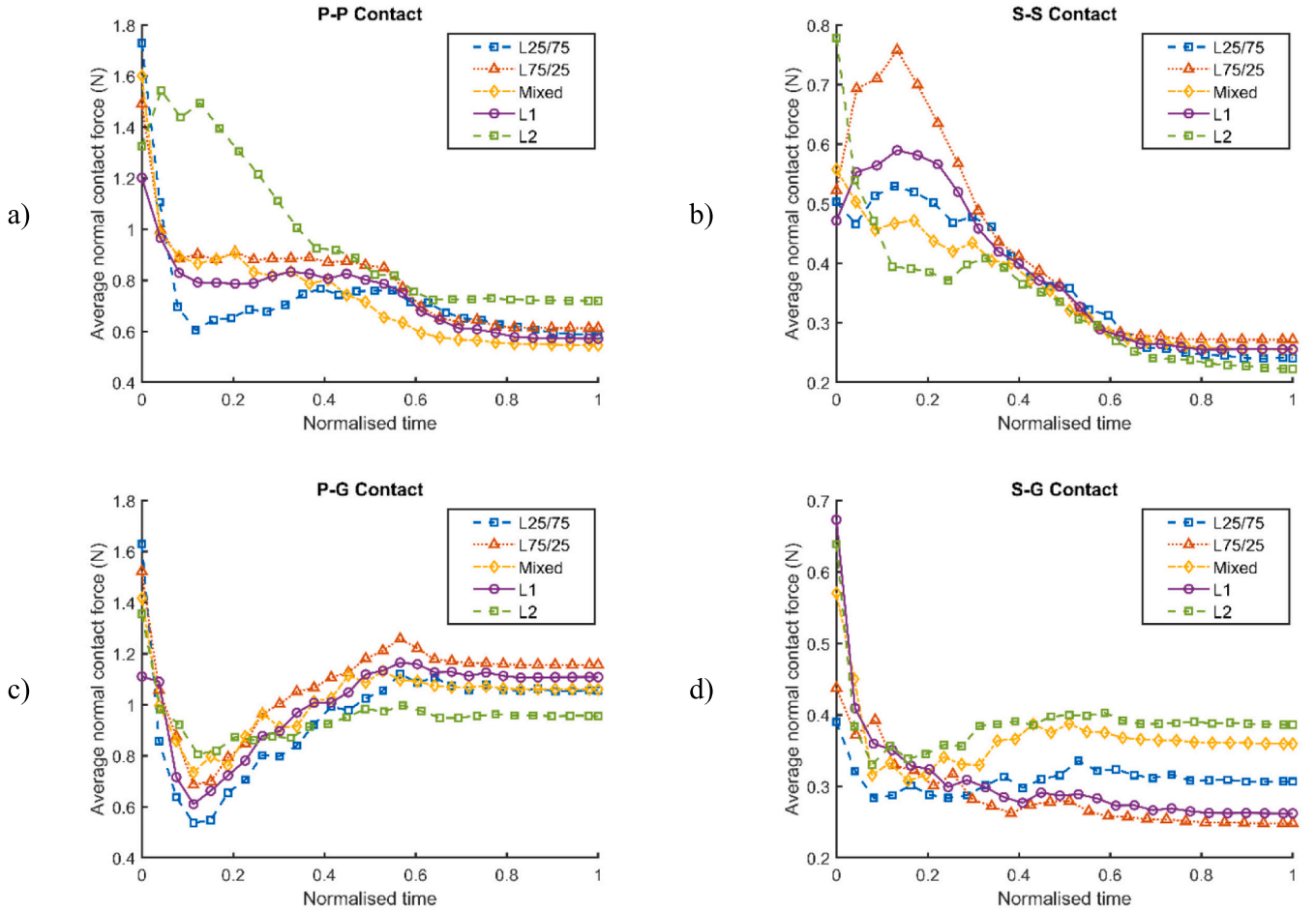

Fig. 15. Average contact force within the heap for different types of contact in various initial configurations. (Abbreviation: P-P = pellet-pellet, S-S = sinter-sinter, P-G = pellet-geometry and S-G = sinter-geometry.)

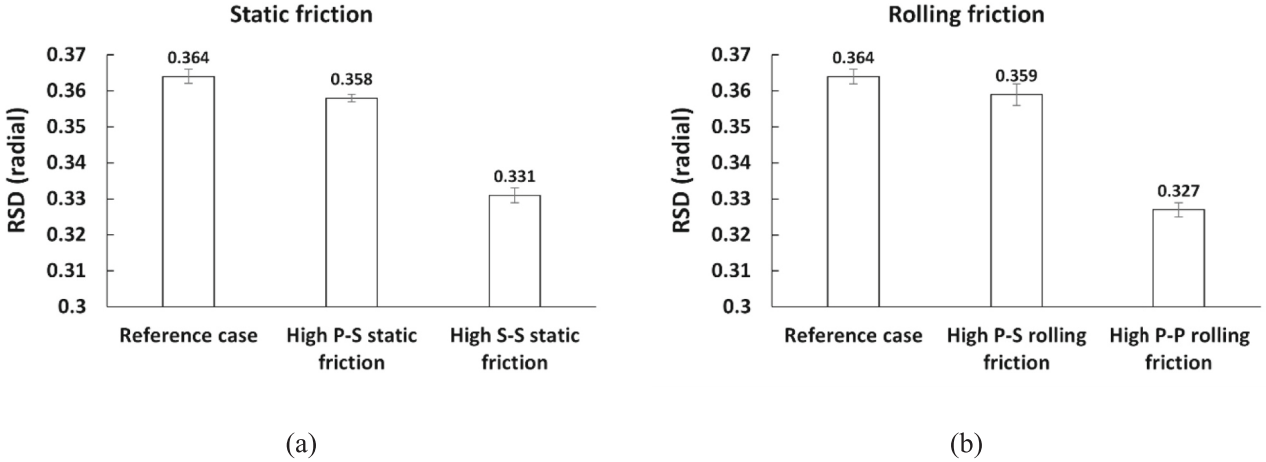

Fig. 16. Comparison between the effect of changing a) pellet-sinter (P-S) and sinter-sinter (S-S) coefficient of static friction, and b) pellet-sinter (P-S) and pellet-pellet (P-P) coefficient of rolling friction on radial segregation in the heap. The value above each bar denotes the mean RSD and the error bar represents the standard deviation from three repetitions.

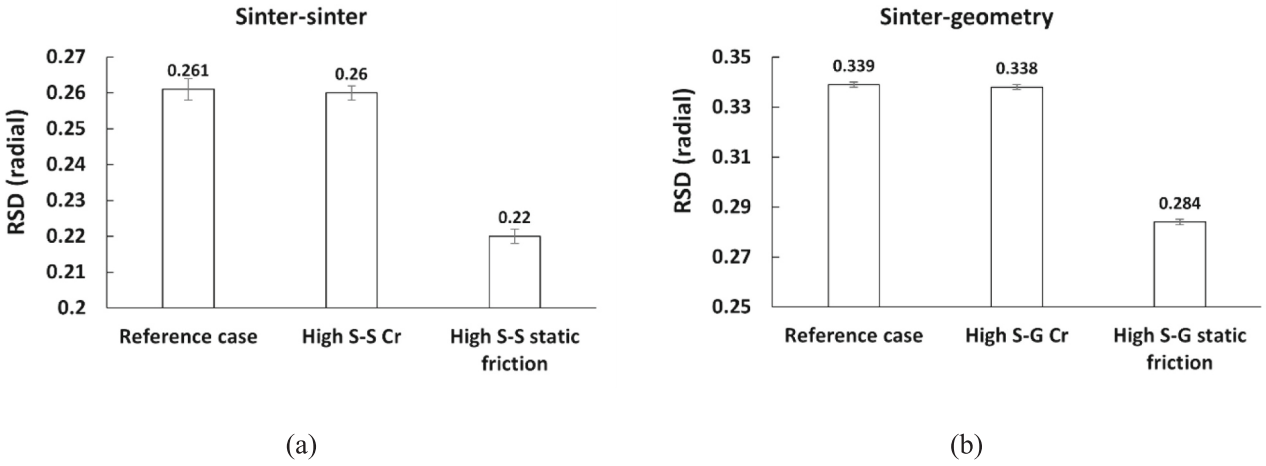

(a) (b)

Fig. 17. Comparison between the effect of changing the coefficient of restitution and static friction on radial segregation for a) sinter-sinter, and b) sinter-geometry interactions. The value above each bar denotes the mean RSD and the error bar represents the standard deviation from three repetitions.

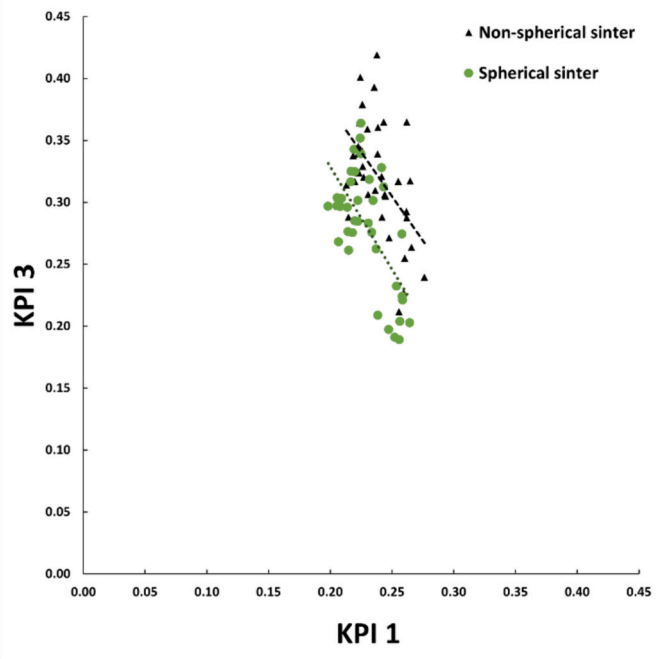

Fig. 18. The effect of the sinter's particle shape on KPI 1 and KPI 3, i.e. segregation after hopper and radial segregation in the heap, respectively (the dashed lines denote linear regression fits.)

correlation coefficient, the plots are qualitatively and quantitatively similar. The main discrepancy is observed only at the first normalised time, when pellets and sinter are mixed on the chute, leading to a lower SI for KPI 2 at time zero. Hence, we conclude that, for the setup and materials being studied in the present work, no significant segregation happens on the chute itself. The authors emphasise that this conclusion is valid within the scope of this study. For instance, significant segregation might occur on the chute if it is sufficiently long, as demonstrated in previous studies [14,52,61]. As a result, within the scope of this study, we proceed with the substantiated assumption that the dominant DEM parameters influencing KPI 1 also have a significant influence on KPI 2.

4.2.2. *Segregation in the heap (KPI 3)*

In this section, we explore the dominant factors influencing heap segregation. As outlined in Section 3.3.2, segregation within the heap is assessed across various directions, namely radial, vertical, and circumferential ones. To identify the most pronounced direction of segregation, we conducted a comparative analysis of RSD across all 37 runs. Fig. 14 presents this comparison for both mixed and L1 configurations in the hopper, revealing a considerably higher degree of segregation in the radial direction compared to the vertical and circumferential directions for both configurations. Therefore, the primary emphasis will be on explaining the key parameters influencing segregation in the radial direction. Throughout the remainder of the paper, we refer to the radial segregation as KPI 3.

Table 4 presents the *p*-values resulting from ANOVA analysis of DSD for radial segregation for all initial configurations within the hopper together with their effect on KPI 3. To better understand these results, it is essential to consider that heap segregation measured at the end of the simulation arises from three main occurrences: 1) segregation present before materials are loaded into the bin (SL3), 2) segregation occurring at the start of material charging into the bin due to particle-geometry interactions, and 3) segregation during heap formation, primarily influenced by particle-particle interactions. Given that the first two occurrences are mainly influenced by particle-geometry interactions, we anticipate that particle-geometry parameters are dominant for KPI 3. This is reflected in Table 4 where particle-geometry interactions were found to be significant for all configurations. Additionally, particle-particle interaction parameters are also expected to be influential due to the third occurrence, where most interactions happen between particles, which is also reflected in Table 4.

Similar to KPI 1, we attempt to support the statistical findings regarding the significance of the parameters. To achieve this, we illustrate the average normal contact force within the heap for significant interaction parameters (based on Table 4) during the formation of the pile for all initial configurations in Fig. 15. To facilitate comparison, we consider pellet-pellet interactions as an example. As indicated in Table 4, pellet-pellet interaction parameters were found to be significant for all cases except for L25/75. This observation is also reflected in Fig. 15a, where L25/75 exhibits the lowest average normal contact force

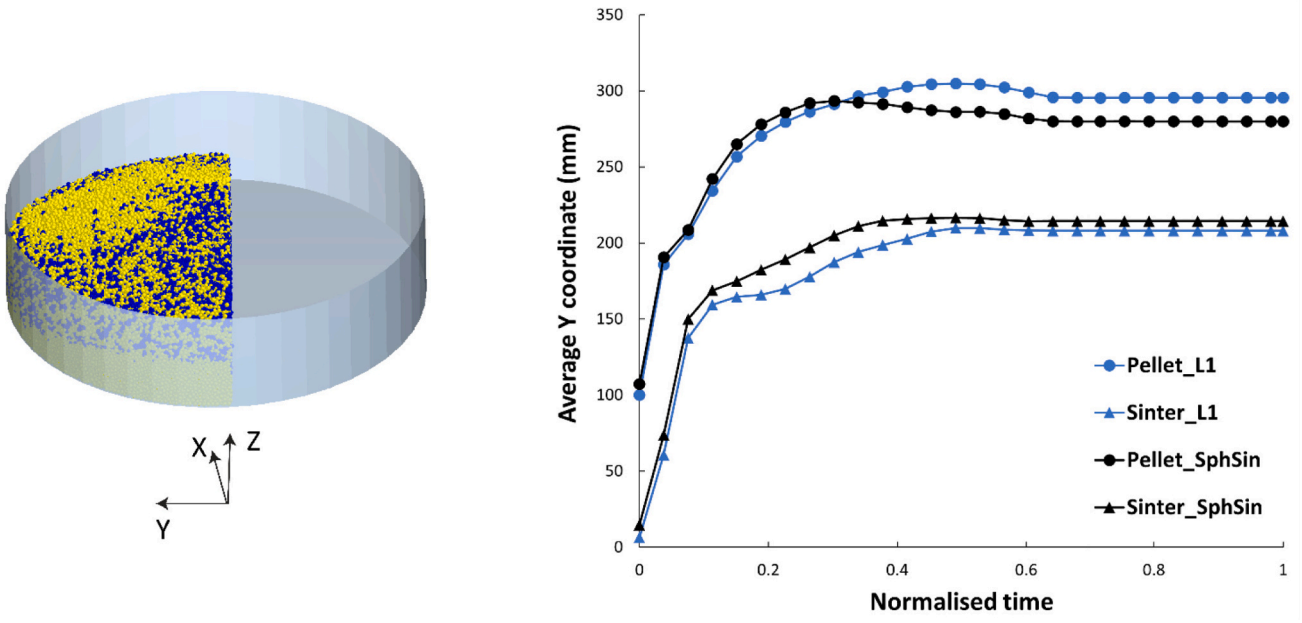

Fig. 19. a) Half of the heap in the Y direction, b) average Y coordinates of pellets and sinter in the half heap for L1 (non-spherical) and spherical sinter particles.

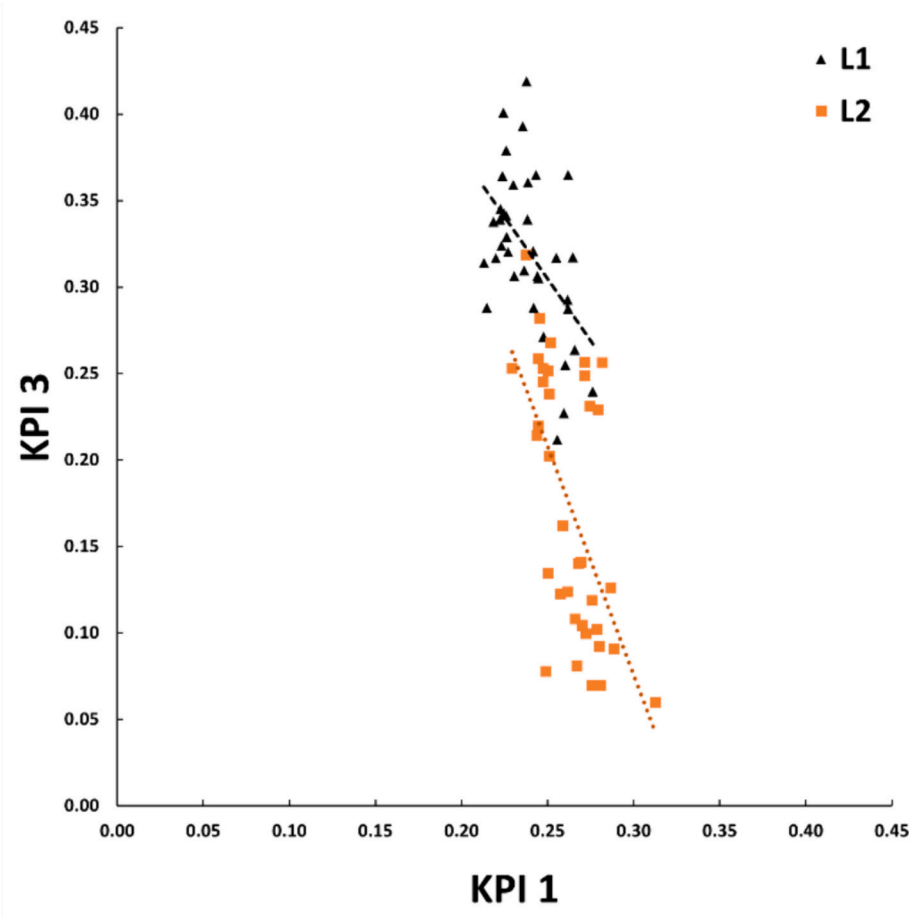

Fig. 20. The effect of layering mode on KPI 1 and KPI 3, i.e. segregation after hopper and radial segregation in the heap, respectively (the dashed lines denote linear regression fits.)

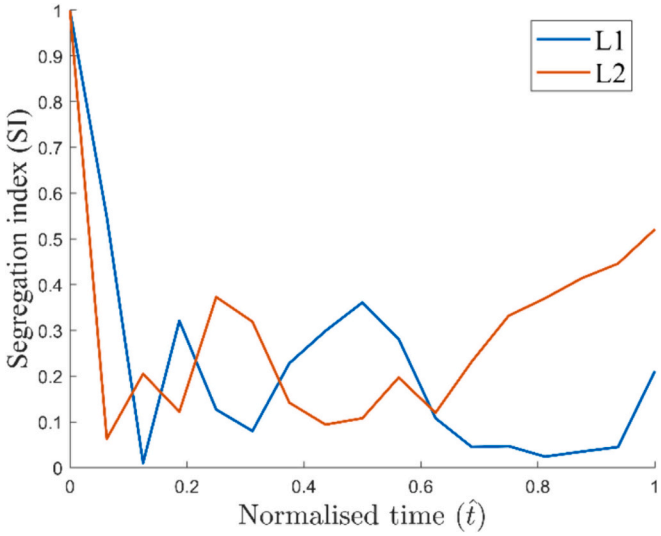

Fig. 21. Comparison of KPI 1 between L1 and L2 cases for Run 36.

for P-P interactions. A similar trend is observed for sinter-sinter interaction, where in Fig. 15b, L2 displays the lowest average normal contact force, which aligns with the higher *p*-value in Table 4 compared to other cases. Hence, this supports the results of the conducted statistical analysis.

In addition to the dominant parameters, we can derive extra insights into the influence of various factors on the dominance of segregation parameters through a detailed analysis of Table 4. These factors include pellet-sinter interaction parameters, pellet-sinter mass ratio, coefficient of restitution, and sinter's rolling friction. These findings will be discussed in the following paragraphs.

Effect of pellet-sinter interaction parameters. Based on Table 4, the impact of the pellet-sinter interaction on radial segregation is statistically insignificant. While previous research has shown the negligible influence of pellet-sinter interaction parameters on the angle of repose [37], there exists a scarcity of studies examining their effects on segregation. To validate this observation, we conducted additional simulations, focusing on the comparison of pellet-sinter interactions with influential parameters (cf. Table 4) such as the sinter-sinter (S-S) coefficient of static friction and the pellet-pellet (P-P) coefficient of rolling friction. We chose Run 9 with the L1 configuration since all mentioned parameters are at their low levels (cf. Table B1). Subsequently, we systematically increased the value of each parameter to the high level (cf. Table 2) individually to observe its impact on radial segregation. The findings, presented in Fig. 16 are inline with Table 4 and confirm that pellet-sinter interaction parameters are insignificant for radial segregation here.

Effect of pellet-sinter mass ratio. To examine the effect of the pellet-sinter mass ratio on the parameter's significance, we compared the dominant parameters between the L1 configuration (i.e., with a mass ratio of 50/50), L75/25, and L25/75 in Table 4. Our findings suggest that the mass ratio has some influence on the dominant parameters for segregation. Although the significance of sinter interaction parameters remains unchanged, the significance of both pellet-pellet and pellet-geometry interactions are affected by changes in pellet mass ratio. Specifically, when the pellet mass ratio is reduced to 25%, both pellet-pellet and pellet-geometry interactions lose their statistical significance.

Effect of the coefficient of restitution (C_r). Table 4 also indicates that the coefficient of restitution (C_r) does not have statistical significance across all observed instances. To confirm this, we attempted to compare the effect of increasing the particle-particle C_r from a low to a high level together with another significant parameter from Table 4. To accomplish this, we selected the coefficient of restitution and coefficient of static friction for sinter-sinter interactions (i.e., $C_{r,ss}$ and $\mu_{s,ss}$). Using the L1 initial configuration within the hopper, we chose Run 5 from Table B1 where both $C_{r,ss}$ and $\mu_{s,ss}$ are at a low level. Subsequently, we conducted two additional simulations, each involving an increase in one of these parameters, to observe the change in radial segregation. We followed a similar approach to compare the influence of increasing the sinter-geometry coefficient of restitution ($C_{r,sg}$) with a significant parameter, sinter-geometry static friction ($\mu_{s,sg}$). For this, we considered Run 10 (cf. Table B1) with the L1 configuration, where both parameters are at a low level. Fig. 17 visually presents the variations in RSD of radial segregation for the mentioned cases. The findings suggest that neither the sinter-sinter nor the sinter-geometry coefficient of restitution significantly affects radial segregation when compared to static friction, which confirms our conclusion regarding the insignificance of the coefficient of restitution for radial segregation.

Effect of the sinter's rolling friction. Although rolling friction of pellet-pellet and pellet-geometry interactions were found to be significant (cf. Table 4), sinter-sinter and sinter-geometry interactions are insignificant. This implies that the chosen particle shape (cf. Fig. 4) based on the literature on segregation [12], can adequately replicate the rolling behaviour of sinter particles in capturing segregation, regardless of the rolling friction's value.

4.3. Effect of initial mixture composition, sinter's particle shape and mass ratio) on segregation

In this section, we examine how the shape of sinter particles, layering mode, and the mass ratio of pellets to sinter, influence segregation. This adds to the previous section (i.e., Section 4.1), which mainly looked at which DEM parameters dominate segregation.

4.3.1. Effect of particle shape on segregation

As noted in Section 2.2.1, we employed a non-spherical particle shape to represent sinter particles (cf. Fig. 4). However, the use of non-spherical particles in the DEM model substantially increases computational time. It would be beneficial to investigate whether using spherical

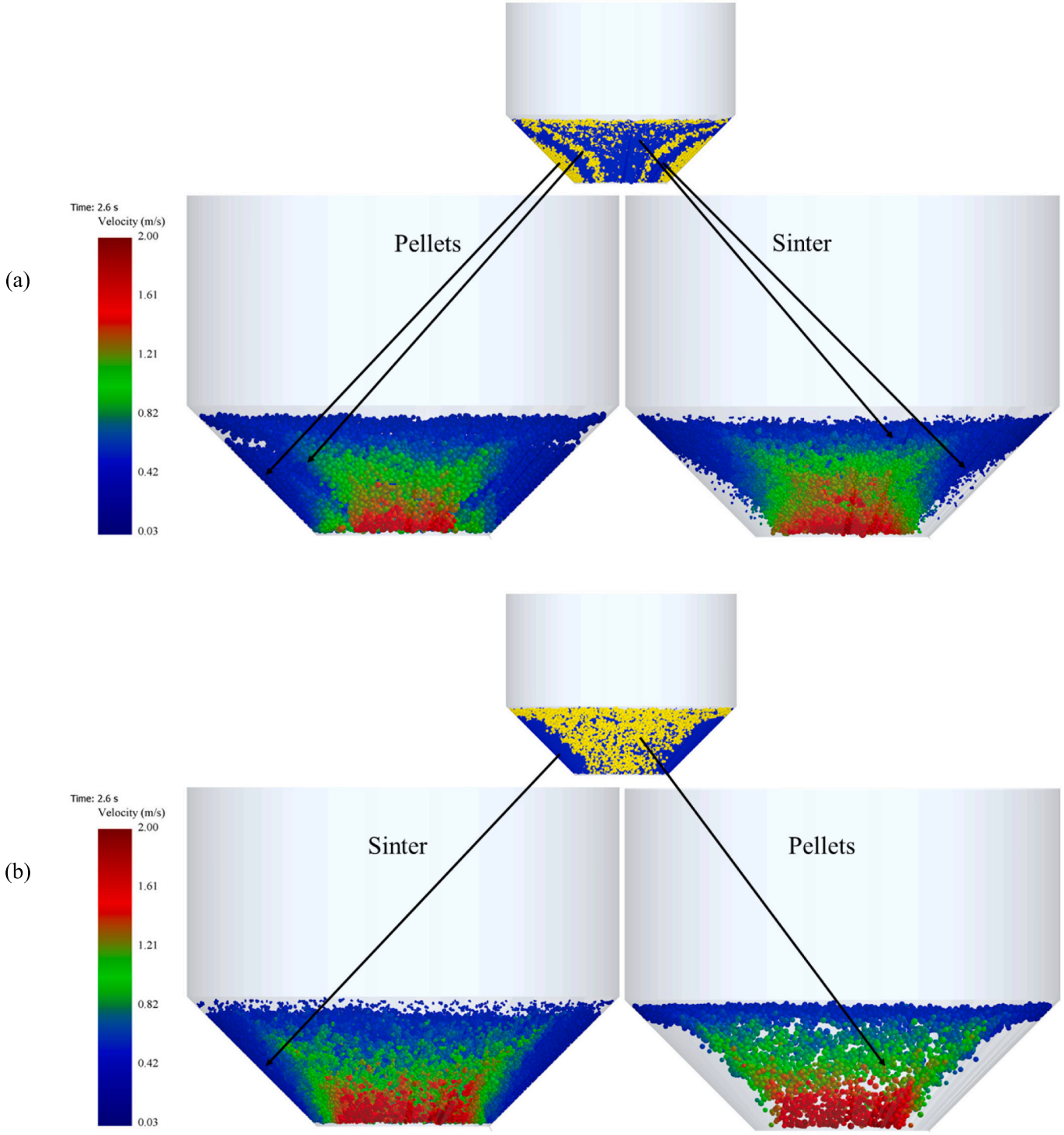

Fig. 22. Velocity profiles within the half-cut hopper for a) L1, and b) L2 initial configurations at $t = 2.6$ s.

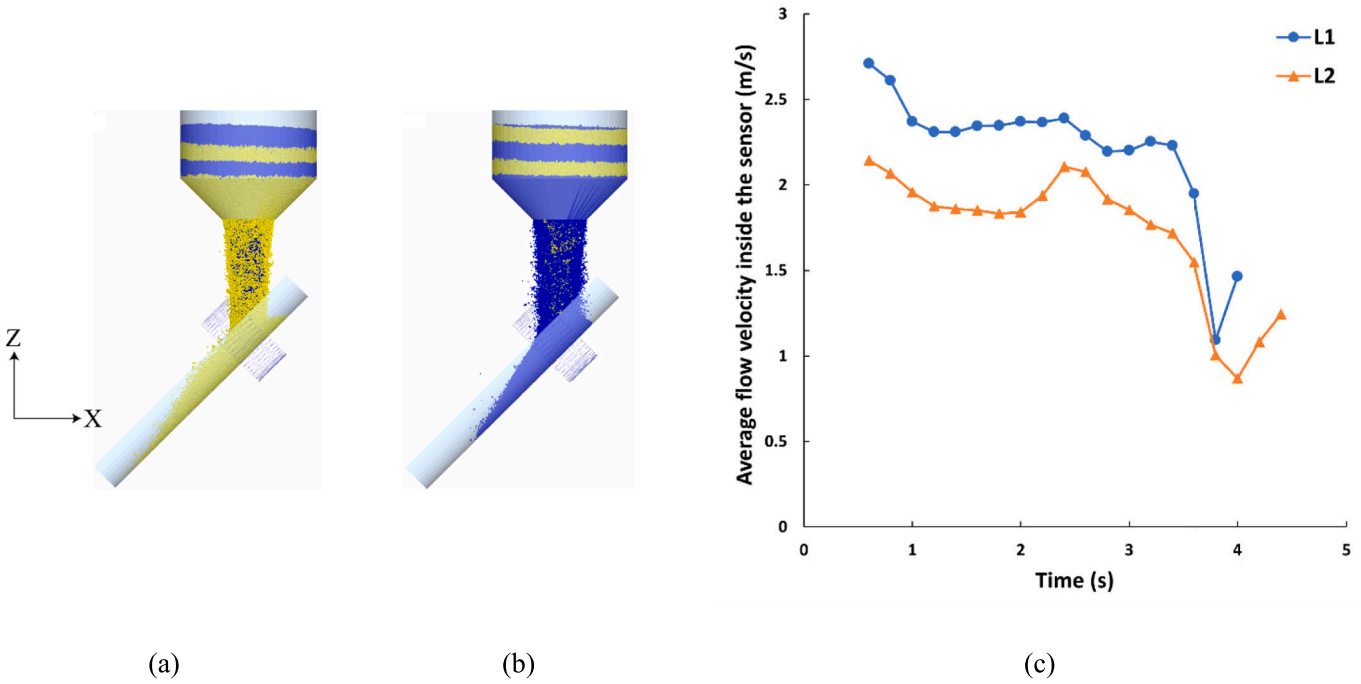

Fig. 23. Snapshots of the simulations showing the flow on the chute at $t = 0.6$ for a) L1 and b) L2 cases, and c) comparison of the average velocity of the flow between L1 and L2 cases.

sinter particles can still accurately capture their segregation behaviour. To investigate this, we conducted an additional set of simulations using volume-equivalent spheres to model sinter, specifically to investigate the effects of particle shape on segregation.

Fig. 18 illustrates the results regarding the segregation after the hopper discharge (KPI 1) and the radial segregation in the heap (KPI 3) for spherical and non-spherical sinter particle cases across all runs. Notably, particle shape seems to have a more significant effect on KPI 3 compared to KPI 1. To quantitatively assess the effect of sinter's particle shape on both KPIs, we used Cohen's d [62]. This is a statistical metric for evaluating the effect size, or the magnitude of difference, between two sets of data. Cohen's d is computed as follows:

$$d = \frac{\bar{x}_1 - \bar{x}_2}{s} \tag{7}$$

where $\bar{x}_1$ and $\bar{x}_2$ represent the means of samples 1 and 2 (equivalent to runs with non-spherical and spherical sinter particles in this study), respectively, and s denotes the pooled standard deviation, calculated as:

$$s = \sqrt{\frac{\sigma_1^2 + \sigma_2^2}{2}} \tag{8}$$

where σ_1 and σ_2 are the standard deviations of samples 1 and 2, respectively. We calculated Cohen's d as 0.48 and 0.87 for the effect of sinter's particle shape on KPI 1 and KPI 3, respectively. According to [62,63], these two Cohen's d values indicate small and large effect sizes, respectively. Hence, we conclude that while changing the sinter's particle shape significantly influences radial segregation in the heap, it has an insignificant impact on the segregation after hopper discharge.

As discussed in Section 4.1.2, the segregation in the heap results from various stages: before materials enter the bin (during hopper discharge and on the chute), during the initial charging into the bin where interactions with the geometry are dominant, and when materials interact with each other on the heap surface. Since particle shape does not significantly impact the segregation before materials enter the bin (cf. Fig. 18), we focus on the two subsequent causes to understand the role of particle shape.

Radial segregation stems from differences in the X and Y coordinates between pellets and sinter (cf. Fig. 19a). To further explore this, we extracted the average Y coordinates of pellets and sinter within half of the heap, given its symmetry in the Y direction (see Fig. 19a). We take Run 12 as an example, which exhibits the highest difference in RSD. Fig. 19b illustrates the average Y for pellets and sinter inside the heap for L1 (i.e., with non-spherical sinter particles) and spherical sinter particles. The graph reveals a greater deviation in the Y coordinates of pellets and sinter in the case of L1, indicating higher radial segregation. This could be attributed to two factors: first, spherical sinter particles exhibit higher rollability than non-spherical ones, causing them to roll more towards the sides of the heap and resulting in a higher Y; and second, in the case of L1, where the rollability of non-spherical sinter particles is less than that of (spherical) pellets, the non-spherical sinter particles tend to remain close to the centre of the heap, allowing pellets to roll over them towards the sides, leading to higher Y coordinates for pellets compared to the case of spherical sinter particles.

4.3.2. *Effect of layering mode on segregation*

Similar to the effect of particle shape, we seek to examine how the layering mode influences segregation by comparing cases L1 and L2 (cf. Fig. 6). Fig. 20 shows how the layering mode affects segregation after hopper discharge (KPI 1) as well as radial segregation in the heap (KPI 3). Similar to the influence of sinter particle shape, the layering mode has a more significant effect on KPI 3 compared to KPI 1. We used Cohen's d (cf. Eq. (7)) to quantitatively assess these effects, resulting in

(a)

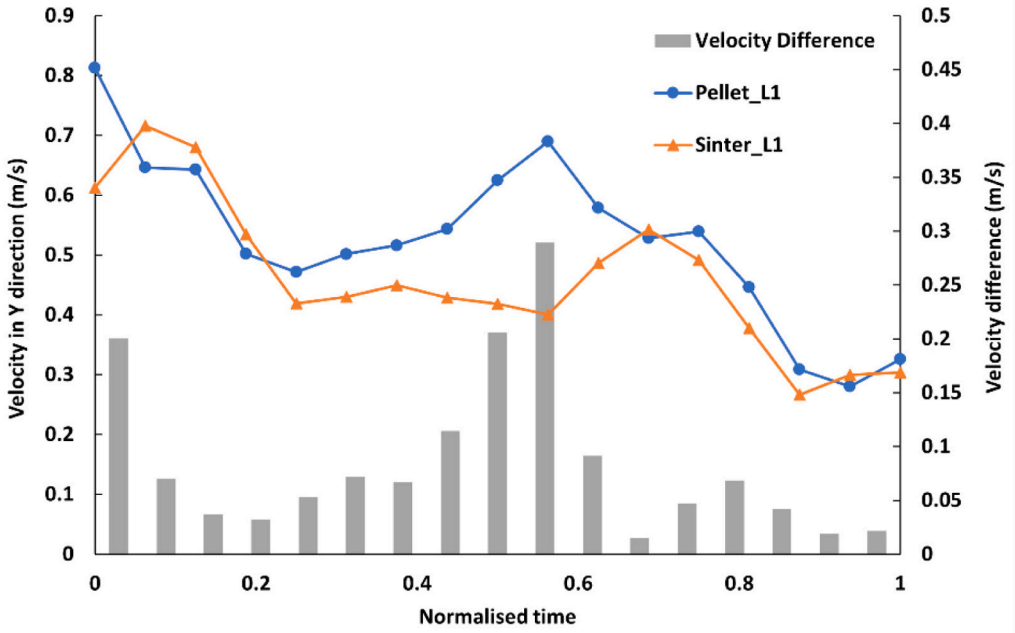

(b)

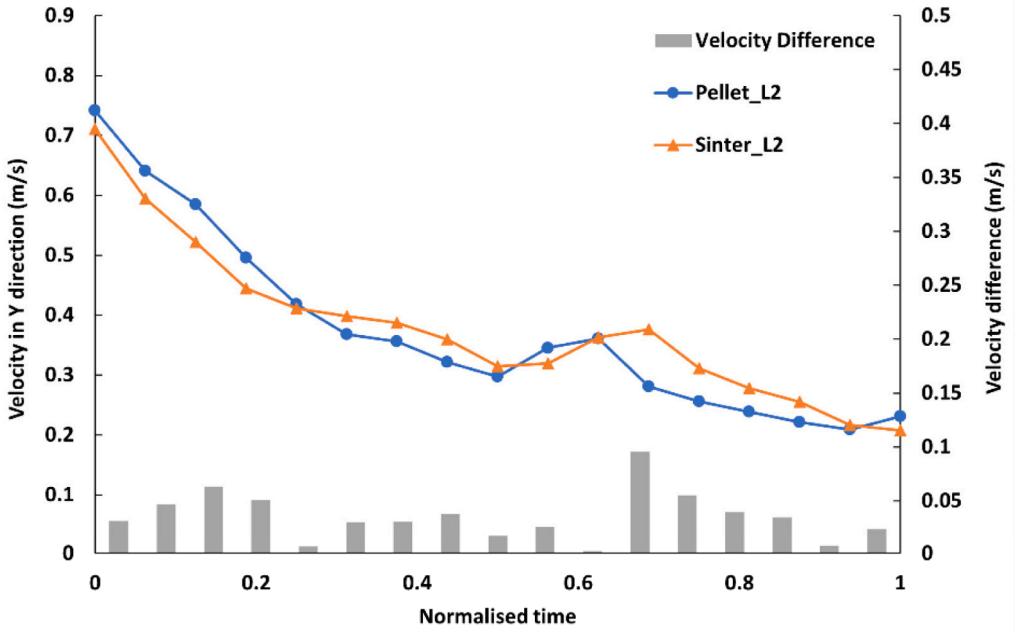

Fig. 24. The velocity of the pellets and sinter in the Y direction during the heap formation for a) L1 and b) L2 cases.

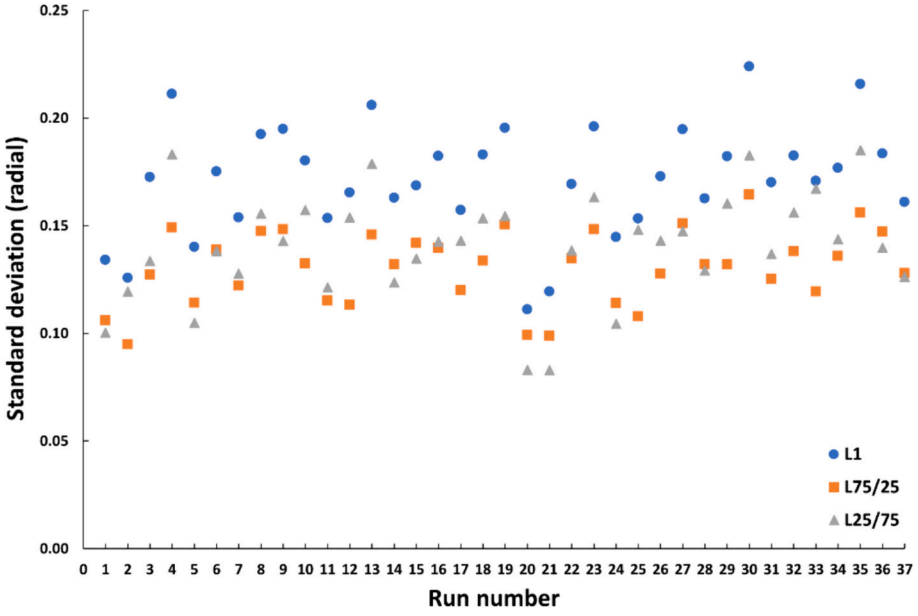

Fig. 25. The standard deviation (SD) for L1 (50/50), L75/25 and L25/75 across all runs.

Table 5
Results of Cohen's d effect size regarding the effect of mass ratio on radial segregation in the heap.

Configuration tested for Cohen's d test	Cohen's d	Interpretation
L1 & L75/25	1.87	Very large effect size
L1 & L25/75	1.2	Very large effect size
L75/25 & L25/75	0.47	Small effect size

Table 6
Summary of the significance of various DEM interaction parameters for different KPIs across all hopper filling configurations. The arrow (↑) indicates the significant parameter. "(+)" and "(−)" show a positive and negative correlation with KPI, respectively. "±" indicates that the parameter correlation can vary depending on the hopper filling configuration. "x" denotes no significant effect on the KPI. Abbreviation: P-P = pellet-pellet, S-S = sinter-sinter, P-S = pellet-sinter, P-G = pellet-geometry and S-G = sinter-geometry.

KPI	P-P	S-S	P-S	P-G	S-G
KPI 1 (segregation after the hopper discharge) and KPI 2 (segregation after chute flow)*	x	↑ (+)	x	↑ (±)	↑ (±)
KPI 3 (segregation in the radial direction of the heap)**	↑ (+)	↑ (±)	x	↑ (−)	↑ (−)

* cf. Fig. 7b.
** cf. Fig. 9a.

Table 7
Summary of the effect of sinter's particle shape, layering mode and pellet-sinter mass ratio on KPIs. "x" denotes no significant effect on the KPI. The arrow (↑) indicates a significant effect.

KPI	Sinter's particle shape	Layering mode	Pellet-sinter mass ratio
KPI 1 (segregation after the hopper discharge) and KPI 2 (segregation after chute flow)*	x	↑ L2 configuration (cf. Fig. 6) leads to more segregation than L1.)**	NA
KPI 3 (segregation in the radial direction of the heap)***	↑ (Using spherical particles for sinter leads to less segregation.)	↑ (L2 configuration (cf. Fig. 6) leads to less segregation than L1.)	↑ (A 50%–50% mass ratio of pellets and sinter results in the highest segregation compared to 75%–25% and 25%–75% mass ratios.)

* cf. Fig. 7b.
** See Fig. 6 for L1 and L2.
*** cf. Fig. 9a.

1.45 and 2.34 for the effect of layering mode on KPI 1 and KPI3, respectively. According to [62,63], these values indicate a huge effect size. Hence, we conclude that layering mode significantly influences both KPI 1 and KPI 3.

To understand the reason behind the impact of the layering mode on KPI 1, we compared the segregation occurring after the hopper between L1 and L2 cases for Run 36 which has the highest effect of the layering mode. The comparison, presented in Fig. 21, highlights that the main difference between L1 and L2 occurs at the end of hopper discharge, i.e., after the normalised time of 0.6 (equivalent to the simulation time of 2.4 s).

To explore this further, we examined the velocity profiles of pellets and sinter within the half-cut hopper for both L1 and L2 configurations, focusing on Run 36, as shown in Fig. 22. A comparison of Fig. 22a and Fig. 22b on the left reveals that in L1, two distinct layers of pellets are being discharged alongside sinter particles, preventing segregation. However, in L2, the high rolling resistance between the bottommost layer of the sinter and the geometry prevents the discharge of sinter particles, while the majority of pellets have already been discharged. Consequently, at the end of the hopper discharging, the mixture is predominantly composed of sinter particles, resulting in a high segregation index (SI), as shown in Fig. 21. Therefore, we conclude that the main reason behind the layering effect is the difference in the rolling behaviour of pellets and sinter particles. This elucidates why in certain runs such as 8, 17 and 35, where pellets have high rolling friction, the effect of layering mode on KPI 1 is minimal.

Regarding the effect of the layering mode on KPI 3, Fig. 20 illustrates that in most runs L2 leads to less segregation. Two main reasons contribute to this observation. First, in the case of L2, sinter particles exit

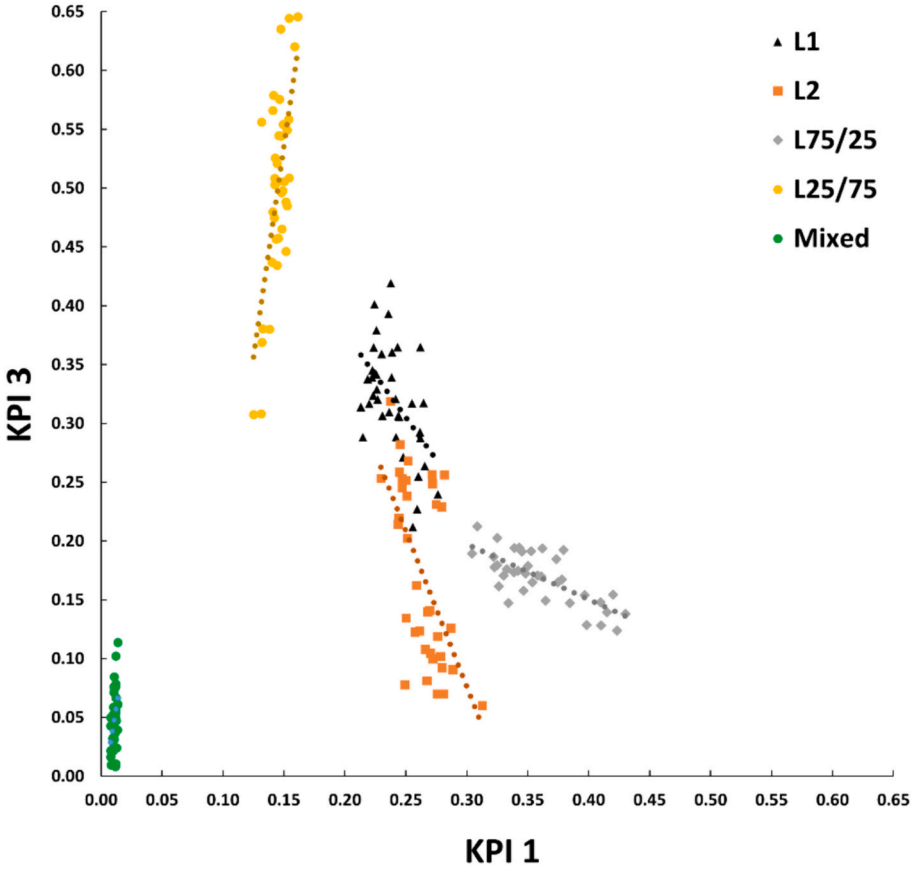

Fig. 26. The relationship between KPI 3 and KPI 1 based on the results obtained in this study for all hopper filling configurations.

the hopper first and fall onto the chute. Due to the lower flowability of sinter particles on the chute, the flow velocity of particles decreases, causing a semi-blockage of the flow. Fig. *23* presents snapshots of the flow on the chute for both L1 and L2, accompanied by the average velocity measured at the velocity sensor located at the beginning of the chute. The comparison in Fig. *23*c reveals a significant difference in the flow velocity between L1 and L2, with L2 exhibiting lower velocities. This reduced velocity in L2, not only results in better mixing of pellets and sinter on the chute but also generally reduces the segregation afterwards.

Second, during the process of materials charging into the bin to form the heap, any velocity difference between pellets and sinter could contribute to radial segregation. Since the heap is symmetric in the Y direction, as illustrated in Fig. 19a, we extracted the velocity of pellets and sinter in the Y direction for half of the heap, as shown in Fig. 24. The observed difference in velocity in the Y direction is higher for L1 between the normalised time of 0.2 and 0.6 (cf. Fig. 24a), primarily due to the higher velocity of pellets.

In the case of L1, the bottom layer of the heap, which is in direct contact with the geometry, contains pellets. Because of their spherical shape, pellets have a high tendency to roll and be pushed towards the edge of the bin as more materials are charged into the bin, resulting in higher velocity in the Y direction for pellets in L1. However, in L2, the bottom layer mostly consists of sinter particles surrounding the pellets, preventing easy sliding and rolling of pellets towards the edge. Once the pellets reach the edge of the bin in L1 (around the normalised time of 0.56), the velocity of pellets starts to decline.

Therefore, we conclude that the difference in sliding and rolling friction between pellets and sinter is the main reason for the effect of layering mode on radial segregation. This clarifies why in Runs 2, 7, and 29 (cf. Table B1), where pellets and sinter have similar rolling and sliding characteristics (i.e., low S-G and high P-G sliding and rolling friction), have minimal radial segregations.

4.3.3. *Effect of mass ratio on segregation*

Here, we aimed to investigate the effect of the pellets-sinter mass ratio on radial segregation in the heap. Due to the division of the standard deviation by the mean in Eq. (4), using RSD to assess the effect of mass ratio on segregation may lead to misleading interpretations. Therefore, we used the standard deviation (denoted as σ in Eq. (4)) for comparison purposes. Fig. 25 illustrates the standard deviation (σ) for three cases: L1 (with an initial mass ratio of 50–50), L75/25, and L25/75, across all 37 runs.

We once again used Cohen's d (cf. Eq. (7)) to quantitatively evaluate the size effect of the pellet-sinter mass ratio on σ. We calculated Cohen's d for three possible pairs, as reported in Table 5. The results indicate that changing the mass ratio of pellets from 50% (i.e. L1) to either 75% or 25% significantly influences the radial segregation (σ). However, changing pellets' mass ratio from 25% to 75% has an insignificant effect on σ. Additionally, Fig. 25 shows that while L1 consistently demonstrates the highest segregation across all runs, the trend between L75/25 and L25/75 is not consistent.

4.4. *Summary of the results*

In this section, we provide a summary of the findings from this study regarding both the dominant DEM interaction parameters for KPIs and the effect of specific factors on segregation in Table 6 and Table 7, respectively. It is important to note that the results provided in Table 6 offer a broad overview. That is, the significance of the parameters and their correlation with KPIs vary depending on the hopper filling configurations (cf. Fig. 6).

Additionally, Fig. 26 provides a comprehensive overview of the results of this study. It illustrates the relationship between KPI 1 and KPI 3

across all hopper filling configurations. The plot reveals possible correlations between these two KPIs, suggesting the possibility of predicting KPI 3 based on KPI 1. Essentially, it shows that the segregation occurring downstream is influenced by both the degree of segregation present upstream and the filling configurations of the discharge hopper.

5. Conclusion

In this study, we identified the dominant DEM parameters influencing multi-component segregation under various flow conditions and initial configurations of the mixture. We did this for a mixture of pellets and sinter and quantified segregation at distinct stages, using blast furnace processes as studied case: after hopper discharge (KPI 1), after chute flow (KPI 2), and in the static heap (KPI 3). Additionally, we expanded the investigation to assess the effect of certain factors, such as the shape of sinter particles, initial layering mode, and pellet-sinter mass ratio on KPIs. The conclusions of this work are as follows:

- Particle-geometry interaction parameters predominantly influence the segregation after hopper discharge (KPI 1). Particle-particle interaction parameters appear to be insignificant for KPI 1. Furthermore, within the scope of this study, no significant segregation occurs on the chute itself.
- In the heap, the segregation occurring in the radial direction is significantly higher than in the vertical and circumferential directions. For radial segregation (i.e. KPI 3), both particle-geometry and particle-particle interaction can be significant depending on the initial configuration.
- The hopper filling configuration significantly affects both dominant DEM parameters and the extent of segregation. Shifting from L1 to L2 (i.e. changing the bottommost particle from pellets to sinter) not only makes sinter-geometry parameters significant but also reduces radial segregation in the heap. Additionally, varying the mass ratio affects parameter dominance; for example, reducing the pellet mass ratio from 50% to 25% diminishes pellet-pellet interaction significance. Moreover, the 50%–50% mixture shows the highest segregation level.
- Pellet-sinter interaction parameters, as well as the coefficient of restitution (C_r) for all the interactions, were determined to be insignificant for all KPIs.

These conclusions are valid within the specific scope investigated in this work. We emphasise that the overall upstream flow condition is crucial in the segregation downstream. While the insights gained provide valuable contributions to our understanding of granular segregation dynamics, the generalisability of these results requires confirmation through additional research by considering a wider array of hopper filling configurations, incorporating various geometrical properties of the system and exploring other materials properties (e.g., different size distributions). Overall, the results of this study will facilitate more efficient and robust calibration of multi-component models in future research works.

CRediT authorship contribution statement

Ahmed Hadi: Writing – review & editing, Writing – original draft, Visualization, Validation, Software, Methodology, Investigation, Formal analysis, Data curation, Conceptualization. **Hao Shi:** Writing – review & editing, Writing – original draft, Visualization, Validation, Methodology, Investigation, Conceptualization. **Yusong Pang:** Writing – review & editing, Visualization, Supervision, Conceptualization. **Dingena Schott:** Writing – review & editing, Visualization, Validation, Supervision, Resources, Project administration, Methodology, Investigation, Formal analysis, Data curation, Conceptualization.

Declaration of competing interest

The authors declare that they have no known competing financial interests or personal relationships that could have appeared to influence the work reported in this paper.

Data availability

Data will be made available on request.

Acknowledgements

This research was carried out under project number T18019 in the framework of the Research Program of the Materials innovation institute (M2i) (www.m2i.nl) supported by the Dutch government.

The authors would like to acknowledge dr.ir. Jan van der Stel and dr. ir. Allert Adema from Tata Steel Ijmuiden for providing insight and expertise that greatly supported the research.

Appendix A. All DEM parameters used in this study

Table A1
A comprehensive overview of DEM parameters used.

DEM Parameter	Pellet	Sinter	Geometry
Particle shape			NA
Particle size distribution	10–12.5 (mm): 32.8% 12.5–16 (mm): 67.2%	5.6–8 (mm): 14% 8–10 (mm): 22.2% 10–12.5 (mm): 25.9% 12.5–16 (mm): 21.3% 16–20 (mm): 12.2% 20–25 (mm): 4.4%	NA
Shear modulus (G)	1e+8 Pa [37]	1e+8 Pa [37]	2e+11 Pa [41]
Poisson's ratio (υ)	0.25 [37]	0.25 [37]	0.3 [41]
Solid density (ρ_s)	1951 (kg/m^3)	1731 (kg/m^3)	7800 (kg/m^3) [41]

(*continued on next page*)

Table A1 (*continued*)

DEM Parameter	Pellet	Sinter	Geometry
Coefficient of static friction (μ_s)			
Coefficient of rolling friction (μ_r)	Variable (see Table 2)		
Coefficient of restitution (C_r)			
Time step	7.94e-6 s (20% of Rayleigh time step)		

Appendix B. The matrix for definitive screening design (DSD)

Table B1
Definitive screening design matrix.

Run	$\mu_{s,pp}$	$\mu_{r,pp}$	$C_{r,pp}$	$\mu_{s,ss}$	$\mu_{r,ss}$	$C_{r,ss}$	$\mu_{s,ps}$	$\mu_{r,ps}$	$C_{r,ps}$	$\mu_{s,pg}$	$\mu_{r,pg}$	$C_{r,pg}$	$\mu_{s,sg}$	$\mu_{r,sg}$	$C_{r,sg}$
1	0.21	0.05	0.7	0.76	0.08	0.01	0.21	0.38	0.01	0.5	0.35	0.41	0.9	0.2	0.05
2	0.21	0.145	0.7	0.76	0.08	0.35	0.21	0.05	0.01	0.5	0.35	0.2	0.38	0.08	0.5
3	0.7	0.05	0.3	0.76	0.08	0.35	0.76	0.38	0.01	0.31	0.35	0.62	0.9	0.08	0.5
4	0.21	0.05	0.7	0.43	0.38	0.35	0.485	0.38	0.7	0.31	0.35	0.2	0.38	0.08	0.5
5	0.21	0.05	0.3	0.43	0.38	0.01	0.76	0.38	0.355	0.5	0.35	0.2	0.9	0.08	0.05
6	0.7	0.145	0.3	0.43	0.38	0.01	0.76	0.38	0.7	0.31	0.05	0.62	0.9	0.2	0.05
7	0.21	0.24	0.3	0.76	0.38	0.18	0.76	0.38	0.01	0.5	0.05	0.2	0.38	0.2	0.5
8	0.7	0.24	0.7	0.76	0.08	0.35	0.21	0.05	0.355	0.31	0.05	0.62	0.38	0.2	0.5
9	0.21	0.05	0.3	0.43	0.38	0.35	0.21	0.05	0.01	0.5	0.05	0.62	0.9	0.14	0.5
10	0.21	0.24	0.5	0.76	0.38	0.01	0.76	0.05	0.01	0.31	0.35	0.62	0.38	0.08	0.05
11	0.21	0.24	0.7	0.43	0.08	0.01	0.76	0.05	0.7	0.5	0.2	0.62	0.9	0.08	0.5
12	0.21	0.24	0.3	0.43	0.08	0.35	0.21	0.38	0.7	0.405	0.35	0.62	0.38	0.2	0.05
13	0.7	0.24	0.3	0.43	0.38	0.35	0.76	0.05	0.7	0.31	0.05	0.41	0.38	0.08	0.5
14	0.7	0.05	0.7	0.76	0.38	0.01	0.76	0.05	0.01	0.405	0.05	0.2	0.9	0.08	0.5
15	0.21	0.05	0.7	0.76	0.23	0.35	0.76	0.05	0.7	0.31	0.05	0.2	0.9	0.2	0.05
16	0.7	0.05	0.5	0.43	0.08	0.35	0.21	0.38	0.7	0.5	0.05	0.2	0.9	0.2	0.5
17	0.7	0.24	0.3	0.43	0.23	0.01	0.21	0.38	0.01	0.5	0.35	0.62	0.38	0.08	0.5
18	0.21	0.24	0.7	0.43	0.38	0.01	0.21	0.05	0.7	0.5	0.05	0.2	0.38	0.2	0.05
19	0.7	0.05	0.3	0.76	0.38	0.35	0.21	0.38	0.01	0.31	0.2	0.2	0.38	0.2	0.05
20	0.7	0.24	0.3	0.76	0.38	0.35	0.21	0.05	0.7	0.5	0.35	0.2	0.9	0.08	0.05
21	0.455	0.24	0.7	0.76	0.38	0.35	0.76	0.38	0.7	0.5	0.35	0.62	0.9	0.2	0.5
22	0.21	0.24	0.3	0.76	0.08	0.01	0.21	0.38	0.7	0.31	0.05	0.2	0.9	0.08	0.5
23	0.7	0.05	0.7	0.43	0.08	0.18	0.21	0.05	0.7	0.31	0.35	0.62	0.9	0.08	0.05
24	0.7	0.24	0.3	0.76	0.08	0.01	0.485	0.05	0.01	0.5	0.05	0.62	0.9	0.2	0.05
25	0.7	0.05	0.3	0.595	0.08	0.01	0.76	0.05	0.7	0.5	0.35	0.2	0.38	0.2	0.5
26	0.455	0.145	0.5	0.595	0.23	0.18	0.485	0.215	0.355	0.405	0.2	0.41	0.64	0.14	0.275
27	0.7	0.24	0.7	0.43	0.38	0.01	0.21	0.215	0.01	0.31	0.35	0.2	0.9	0.2	0.5
28	0.7	0.05	0.7	0.76	0.38	0.01	0.21	0.38	0.7	0.5	0.05	0.62	0.38	0.08	0.275
29	0.7	0.24	0.7	0.76	0.08	0.01	0.76	0.38	0.7	0.31	0.35	0.2	0.38	0.14	0.05
30	0.455	0.05	0.3	0.43	0.08	0.01	0.21	0.05	0.01	0.31	0.05	0.2	0.38	0.08	0.05
31	0.7	0.24	0.7	0.43	0.08	0.35	0.76	0.38	0.01	0.5	0.05	0.2	0.64	0.08	0.05
32	0.21	0.05	0.3	0.76	0.08	0.35	0.76	0.215	0.7	0.5	0.05	0.62	0.38	0.08	0.05
33	0.7	0.05	0.7	0.43	0.38	0.35	0.76	0.05	0.01	0.5	0.35	0.62	0.38	0.2	0.05
34	0.21	0.24	0.3	0.43	0.08	0.35	0.76	0.05	0.01	0.31	0.35	0.2	0.9	0.2	0.275
35	0.21	0.05	0.7	0.43	0.08	0.01	0.76	0.38	0.01	0.31	0.05	0.62	0.38	0.2	0.5
36	0.21	0.24	0.7	0.595	0.38	0.35	0.21	0.38	0.01	0.31	0.05	0.62	0.9	0.08	0.05
37	0.21	0.05	0.3	0.76	0.38	0.01	0.21	0.05	0.7	0.31	0.35	0.62	0.64	0.2	0.5

References

[1] P. Richard, M. Nicodemi, R. Delannay, P. Ribière, D. Bideau, Slow relaxation and compaction of granular systems, Nat. Mater. 4 (2005) 121–128, https://doi.org/10.1038/nmat1300.

[2] A. Rosato, C. Windows-Yule, Segregation in Vibrated Granular Systems, 2020, https://doi.org/10.1016/B978-0-12-814199-1.00002-0.

[3] A.D. Rosato, D.L. Blackmore, N. Zhang, Y. Lan, A perspective on vibration-induced size segregation of granular materials, Chem. Eng. Sci. 57 (2002) 265–275, https://doi.org/10.1016/S0009-2509(01)00380-3.

[4] A. Hadi, R. Roeplal, Y. Pang, D.L. Schott, DEM modelling of segregation in granular materials: a review, KONA Powder Part J. (2023), https://doi.org/10.14356/kona.2024017.

[5] W.R. Ketterhagen, B.C. Hancock, Optimizing the design of eccentric feed hoppers for tablet presses using DEM, Comput. Chem. Eng. 34 (2010) 1072–1081, https://doi.org/10.1016/j.compchemeng.2010.04.016.

[6] A. Cliff, L.A. Fullard, E.C.P. Breard, J. Dufek, C.E. Davies, Granular size segregation in silos with and without inserts, Proc. R. Soc. A Math. Phys. Eng. Sci. 477 (2021), https://doi.org/10.1098/rspa.2020.0242.

[7] Y. Yu, H. Saxén, Particle flow and behavior at bell-less charging of the blast furnace, Steel Res. Int. 84 (2013) 1018–1033, https://doi.org/10.1002/srin.201300028.

[8] X. Tian, H. Zhou, J. Huang, S. Wu, G. Wang, M. Kou, DEM study on discharge behavior of ternary cylindrical activated coke particles, Powder Technol. 409 (2022) 117785, https://doi.org/10.1016/j.powtec.2022.117785.

[9] S. Mandal, D.V. Khakhar, Dense granular flow of mixtures of spheres and dumbbells down a rough inclined plane: segregation and rheology, Phys. Fluids 31 (2019) 23304, https://doi.org/10.1063/1.5082355.

[10] Y. Yu, H. Saxén, Experimental and DEM study of segregation of ternary size particles in a blast furnace top bunker model, Chem. Eng. Sci. 65 (2010) 5237–5250, https://doi.org/10.1016/j.ces.2010.06.025.

[11] S. Wu, M. Kou, J. Xu, X. Guo, K. Du, W. Shen, J. Sun, DEM simulation of particle size segregation behavior during charging into and discharging from a Paul-Wurth type hopper, Chem. Eng. Sci. 99 (2013) 314–323, https://doi.org/10.1016/j.ces.2013.06.018.

[12] E. Izard, M. Moreau, P. Ravier, Discrete element method simulation of segregation pattern in a sinter cooler charging chute system, Particuology 59 (2021) 34–42, https://doi.org/10.1016/j.partic.2020.08.004.

[13] M. Combarros Garcia, H.J. Feise, S. Strege, A. Kwade, Segregation in heaps and silos: comparison between experiment, simulation and continuum model, Powder Technol. 293 (2016) 26–36, https://doi.org/10.1016/j.powtec.2015.09.036.
[14] T. Bhattacharya, J.J. McCarthy, Chute flow as a means of segregation characterization, Powder Technol. 256 (2014) 126–139, https://doi.org/10.1016/j.powtec.2014.01.092.
[15] H. Mio, S. Komatsuki, M. Akashi, A. Shimosaka, Y. Shirakawa, J. Hidaka, M. Kadowaki, S. Matsuzaki, K. Kunitomo, Effect of chute angle on charging behavior of sintered ore particles at bell-less type charging system of blast furnace by discrete element method, ISIJ Int. 49 (2009) 479–486, https://doi.org/10.2355/ISIJINTERNATIONAL.49.479.
[16] H. Mio, M. Kadowaki, S. Matsuzaki, K. Kunitomo, Development of particle flow simulator in charging process of blast furnace by discrete element method, Miner. Eng. (2012) 27–33, https://doi.org/10.1016/j.mineng.2012.01.002.
[17] M. Kou, S. Wu, G. Wang, B. Zhao, Q. Cai, Numerical simulation of burden and gas distributions inside COREX shaft furnace, Steel Res. Int. 86 (2015) 686–694, https://doi.org/10.1002/srin.201400311.
[18] M. Kou, J. Xu, H. Zhou, B. Wen, K. Gu, S. Yao, S. Wu, Effects of bottom base shapes on burden profiles and burden size distributions in the upper part of a COREX shaft furnace based on DEM, Adv. Powder Technol. 29 (2018) 1014–1024, https://doi.org/10.1016/j.apt.2018.01.020.
[19] M. Asachi, M.A. Behjani, E. Nourafkan, A. Hassanpour, Tailoring particle shape for enhancing the homogeneity of powder mixtures: experimental study and DEM modelling, Particuology 54 (2021) 58–68, https://doi.org/10.1016/j.partic.2020.03.006.
[20] M. Kou, J. Xu, S. Wu, H. Zhou, K. Gu, S. Yao, B. Wen, Effect of cross-section shape of rotating chute on particle movement and distribution at the throat of a bell-less top blast furnace, Particuology 44 (2019) 194–206, https://doi.org/10.1016/j.partic.2018.07.010.
[21] J.M.N.T. Gray, Particle Segregation in Dense Granular Flows 50, 2018, pp. 407–433, https://doi.org/10.1146/annurev-Fluid-122316-045201.
[22] K. Shlnohara, S.I. Mlyata, Mechanism of density segregation of particles in filling vessels, Ind. Eng. Chem. Process. Des. Dev. 23 (1984) 423–428, https://doi.org/10.1021/i200026a003.
[23] N. Jain, J.M. Ottino, R.M. Lueptow, Regimes of segregation and mixing in combined size and density granular systems: an experimental study, Granul. Matter 7 (2005) 69–81, https://doi.org/10.1007/s10035-005-0198-x.
[24] S.P. Duffy, V.M. Puri, Primary segregation shear cell for size-segregation analysis of binary mixtures, Kona Powder Part. J. 20 (2002) 196–207, https://doi.org/10.14356/kona.2002022.
[25] M. Asachi, E. Nourafkan, A. Hassanpour, A review of current techniques for the evaluation of powder mixing, Adv. Powder Technol. 29 (2018) 1525–1549, https://doi.org/10.1016/j.apt.2018.03.031.
[26] P.A. Cundall, O.D.L. Strack, A discrete numerical model for granular assemblies, Geotechnique 29 (1979) 47–65, https://doi.org/10.1680/geot.1979.29.1.47.
[27] R. Roeplal, Y. Pang, A. Adema, J. van der Stel, D. Schott, Modelling of phenomena affecting blast furnace burden permeability using the discrete element method (DEM) – a review, Powder Technol. 415 (2023), https://doi.org/10.1016/j.powtec.2022.118161.
[28] S. Lommen, D. Schott, G. Lodewijks, DEM speedup: stiffness effects on behavior of bulk material, Particuology 12 (2014) 107–112, https://doi.org/10.1016/j.partic.2013.03.006.
[29] S. Lommen, M. Mohajeri, G. Lodewijks, D. Schott, DEM particle upscaling for large-scale bulk handling equipment and material interaction, Powder Technol. 352 (2019) 273–282, https://doi.org/10.1016/j.powtec.2019.04.034.
[30] C.J. Coetzee, Particle upscaling: calibration and validation of the discrete element method, Powder Technol. 344 (2019) 487–503, https://doi.org/10.1016/j.powtec.2018.12.022.
[31] W.R. Ketterhagen, J.S. Curtis, C.R. Wassgren, B.C. Hancock, Modeling granular segregation in flow from quasi-three-dimensional, wedge-shaped hoppers, Powder Technol. 179 (2008) 126–143, https://doi.org/10.1016/j.powtec.2007.06.023.
[32] T.F. Zhang, J.Q. Gan, D. Pinson, Z.Y. Zhou, Size-induced segregation of granular materials during filling a conical hopper, Powder Technol. 340 (2018) 331–343, https://doi.org/10.1016/j.powtec.2018.09.031.
[33] Z. Zhang, Y. Liu, B. Zheng, P. Sun, R. Li, Local percolation of a binary particle mixture in a rectangular hopper with inclined bottom during discharging, ACS Omega 5 (2020) 20773–20783, https://doi.org/10.1021/acsomega.0c01514.
[34] H.P. Zhu, Z.Y. Zhou, R.Y. Yang, A.B. Yu, Discrete particle simulation of particulate systems: theoretical developments, Chem. Eng. Sci. 62 (2007) 3378–3396, https://doi.org/10.1016/j.ces.2006.12.089.
[35] J. Ai, J.F. Chen, J.M. Rotter, J.Y. Ooi, Assessment of rolling resistance models in discrete element simulations, Powder Technol. 206 (2011) 269–282, https://doi.org/10.1016/j.powtec.2010.09.030.
[36] A. Tripathi, V. Kumar, A. Agarwal, A. Tripathi, S. Basu, A. Chakrabarty, S. Nag, Quantitative DEM simulation of pellet and sinter particles using rolling friction estimated from image analysis, Powder Technol. 380 (2021) 288–302, https://doi.org/10.1016/j.powtec.2020.11.024.
[37] A. Chakrabarty, R. Biswas, S. Basu, S. Nag, Characterisation of binary mixtures of pellets and sinter for DEM simulations, Adv. Powder Technol. 33 (2022), https://doi.org/10.1016/j.apt.2021.11.010.
[38] C.M. Wensrich, A. Katterfeld, Rolling friction as a technique for modelling particle shape in DEM, Powder Technol. 217 (2012) 409–417, https://doi.org/10.1016/j.powtec.2011.10.057.
[39] L.F. Viera Valencia, D. Garcia Giraldo, 済無No Title No Title No Title, Angew. Chem. Int. Ed. 6 (11) (2019) 951–952. https://www.tudelft.nl/dhpc/ark:/44463/DelftBluePhase1.
[40] A.H. Hadi, Y. Pang, D.L. Schott, Calibration of DEM parameters for multi-component segregation, in: ICBMH 2023 14th Int. Conf. Bulk Mater. Storage, Handl. Transp, 2023.
[41] H. Wei, H. Nie, Y. Li, H. Saxén, Z. He, Y. Yu, Measurement and simulation validation of DEM parameters of pellet, sinter and coke particles, Powder Technol. 364 (2020) 593–603, https://doi.org/10.1016/j.powtec.2020.01.044.
[42] C. Hildebrandt, S.R. Gopireddy, R. Scherließ, N.A. Urbanetz, Assessment of material and process attributes' influence on tablet quality using a QbD and DEM combined approach, Powder Technol. 345 (2019) 390–404, https://doi.org/10.1016/j.powtec.2019.01.015.
[43] S.H. Chang, T.T. Teng, N. Ismail, Screening of factors influencing cu(II) extraction by soybean oil-based organic solvents using fractional factorial design, J. Environ. Manag. 92 (2011) 2580–2585, https://doi.org/10.1016/j.jenvman.2011.05.025.
[44] J. Emmerink, A. Hadi, J. Jovanova, C. Cleven, D.L. Schott, Parametric analysis of a double shaft, batch-type paddle mixer using the discrete element method (DEM), Processes 11 (2023), https://doi.org/10.3390/pr11030738.
[45] R. Xia, B. Li, X. Wang, T. Li, Z. Yang, Measurement and calibration of the discrete element parameters of wet bulk coal, Meas. J. Int. Meas. Confed. 142 (2019) 84–95, https://doi.org/10.1016/j.measurement.2019.04.069.
[46] P. Bhalode, M. Ierapetritou, Discrete element modeling for continuous powder feeding operation: calibration and system analysis, Int. J. Pharm. 585 (2020), https://doi.org/10.1016/j.ijpharm.2020.119427.
[47] R.D. Nalawade, K.P. Singh, A.K. Roul, A. Patel, Parametric study and calibration of hysteretic spring and linear cohesion contact models for cohesive soils using definitive screening design, Comput. Part. Mech. 10 (2023) 707–728, https://doi.org/10.1007/s40571-022-00523-4.
[48] Y. Yan, R. Helmons, C. Wheeler, D. Schott, Optimization of a convex pattern surface for sliding wear reduction based on a definitive screening design and discrete element method, Powder Technol. 394 (2021) 1094–1110, https://doi.org/10.1016/j.powtec.2021.09.041.
[49] B. Jones, C.J. Nachtsheim, A class of three-level designs for definitive screening in the presence of second-order effects, J. Qual. Technol. 43 (2011) 1–15, https://doi.org/10.1080/00224065.2011.11917841.
[50] B. Jones, C.J. Nachtsheim, Effective design-based model selection for definitive screening designs, Technometrics 59 (2017) 319–329, https://doi.org/10.1080/00401706.2016.1234979.
[51] T. Mitra, Modeling of Burden Distribution in the Blast Furnace, 2016.
[52] Y. Yu, H. Saxén, Flow of pellet and coke particles in and from a fixed chute, Ind. Eng. Chem. Res. 51 (2012) 7383–7397, https://doi.org/10.1021/ie201362n.
[53] Y. Lu, Z. Jiang, X. Zhang, J. Wang, X. Zhang, Vertical section observation of the solid flow in a blast furnace with a cutting method, Metals (Basel) 9 (2019), https://doi.org/10.3390/met9020127.
[54] H. Mio, S. Komatsuki, M. Akashi, A. Shimosaka, Y. Shirakawa, J. Hidaka, M. Kadowaki, S. Matsuzaki, K. Kunitomo, Validation of particle size segregation of sintered ore during flowing through laboratory-scale chute by discrete element method, ISIJ Int. 48 (2008) 1696–1703, https://doi.org/10.2355/isijinternational.48.1696.
[55] S. Basu, A. Chakrabarty, S. Nag, P. Chaudhary, S. Sinha, T. Jain, M.S. Nainegali, V. A. Rodriguez, L.M. Tavares, Modeling and simulation of mechanical degradation of iron ore sinter in a complex transfer chute system using the discrete element model and a particle breakage model, Powder Technol. 417 (2023), https://doi.org/10.1016/j.powtec.2023.118264.
[56] G.K.P. Barrios, R.M. de Carvalho, A. Kwade, L.M. Tavares, Contact parameter estimation for DEM simulation of iron ore pellet handling, Powder Technol. 248 (2013) 84–93, https://doi.org/10.1016/j.powtec.2013.01.063.
[57] N. Standish, A. Kilic, Comparison of stop-start and continuous sampling methods of studying segregation of materials discharging from a hopper, Chem. Eng. Sci. 40 (1985) 2152–2153, https://doi.org/10.1016/0009-2509(85)87036-6.
[58] D.K. Chibwe, G.M. Evans, E. Doroodchi, B.J. Monaghan, D.J. Pinson, S.J. Chew, Charge material distribution behaviour in blast furnace charging system, Powder Technol. 366 (2020) 22–35, https://doi.org/10.1016/j.powtec.2020.02.048.
[59] G. Di Leo, F. Sardanelli, Statistical significance: p value, 0.05 threshold, and applications to radiomics—reasons for a conservative approach, Eur. Radiol. Exp. 4 (2020), https://doi.org/10.1186/s41747-020-0145-y.
[60] L.M. Moore, D.S. Moore, The basic practice of statistics, Technometrics 38 (1996) 404, https://doi.org/10.2307/1271317.
[61] J. Zhang, J. Qiu, H. Guo, S. Ren, H. Sun, G. Wang, Z. Gao, Simulation of particle flow in a bell-less type charging system of a blast furnace using the discrete element method, Particuology 16 (2014) 167–177, https://doi.org/10.1016/j.partic.2014.01.003.
[62] J. Cohen, Statistical Power Analysis for the Behavioral Sciences, Academic press, 2013.
[63] S.S. Sawilowsky, New effect size rules of thumb, J. Mod. Appl. Stat. Methods 8 (2009) 597–599, https://doi.org/10.22237/jmasm/1257035100.